Shyft and Rasputin: a toolbox for hydrologic simulations on triangular irregular networks.

Olga Silantyeva[1], Ola Skavhaug[2], Bikas C. Bhattarai [1], Sigbjørn Helset[3], Lena M. Tallaksen[1], Magne Nordaas[2], and John F. Burkhart [1,3]

[1]Universitet i Oslo, Oslo, Norway
[2]Expert Analytics AS, Oslo, Norway
[3]Statkraft AS, Oslo, Norway

Correspondence: Olga Silantyeva (olga.silantyeva@geo.uio.no)

Abstract. Terrain topography controls insolation variations at catchment scale. This effects are known to be important in cold and mountainous regions due to high diurnal and seasonal variability in incoming radiation. However, meteorological data in such areas lacks accuracy due to sparse station network and coarse re-analysis grids. Simulation tools that model hydrologic processes at local scales require ways to overcome the lack of accuracy in the observational data, particular at high elevations, so downscaling to cell level is done carefully. With an introduction of irregular triangular networks into distributed hydrologic modelling framework Shyft, steps are taken to account for hillslope-scale terrain structures within scope of operational hydrology. This new functionality allows translation of radiation measurements or re-analysis data onto inclined surfaces improving the predictive power of the model.

Based on the Shyft and Rasputin toolbox we show importance of topographic details such as slope and aspect on predicting snowmelt and rainfall-runoff simulations in snow-covered mountainous region of Himalaya. We conduct the series of experiments for catchments in Narayani area of central Nepal in two steps. First, we demonstrate sensitivity of streamflow simulation to mesh size and shape. The results show that there is an upper limit after which further mesh refinement is not useful for simulations. Second, we incorporate "on the fly" correction of incoming solar radiation depending on surface inclination. The experiments with both coarse and fine tin meshes demonstrate that snow-water equivalent and potential evapotranspiration are directly affected by variations in insolation, with less snow and more evaporation on south-facing slopes. Finally, we perform 10-years of hydrological simulation of Budhi-Gandaki catchment with several model configuration incorporating both proposed features (tins and radiation correction), where we reveal better correspondence of simulated and observed discharge for grid-based solution, which is contradictory to our previous study at Marsyangdi-2 catchment.

This is an unfinished study: the Budhi-Gandaki catchment hydrology has to be analyzed carefully. One of the possible reasons of the unexpected results is a complex precipitation pattern in the catchment, which was not caught by the model properly.

1 Introduction

Importance of terrain topography for hydrologic simulations within Earth-System Models (ESM) at catchment, regional, and global scales is emphasized in the recent review by Fan et al. (2019). Contrasting insolation between sunny and shady slopes is a main factor driving variability in physical processes along hillslopes, and it is well-known that variations in topography create differences in local solar angle and insolation at the surface. However, even measurement of radiation flux is subject to uncertainties due to a number of effects such as clouds and terrain shading. At regional scales the main simulation issue is the existence and quality of radiation measurements in mountainous areas. The meteorological stations networks are typically too sparse and the re-analysis grids are too coarse to correctly capture local topographic variations. Therefore, observational errors, if not compensated by calibration, typically propagate through simulations leading to less robust simulation of important variables in the hydrologic domain, such as snow cover (SC), snow-water equivalent (SWE), evapotranspiration (E) or discharge (Q).

Picard et al. (2020) developed recently a theory on the slope correction for albedo measurements. The authors found "a detectable impact even for nearly flat surfaces, with $1-2^o$ inclination" on measured albedo, caused by differences in illumination between horizontal surfaces and inclined ones, which might affect calculation of surface energy budget. Aguilar et al. (2010) showed E rates to be subject to significant impact resulting from topographic approximation for incoming solar radiation (S). The extensive review by Clark et al. (2011) discusses spatial variability of SWE, putting attention on the importance of variability in near-surface meteorological data, but also the importance of hillslope processes. Carey and Woo (2001) studied impact of hillslope processes on snowmelt and streamflow, stressing the importance of topographic effects for subarctic and subalpine basins, so called "energy-limited areas". Comola et al. (2015) performed a set of modelling experiments virtually rotating the catchment to evaluate how spatial scales of slope/aspect impact insolation for snow-dominated areas in Swiss Alps and concluded that the solar patterns are especially important at small-scales, being averaged out at larger scales.

Triangular Irregular Networks (TIN) are known to be an efficient way to represent surface topography for geographic information systems (GIS) applications (Peuckert et al., 1976), particularly important are Delaunay TINs (Tsai, 1993; Kumar et al., 2009) . Introducing TINs into hydrologic modeling is a way to capture topographic features, but with less computational cost compared to regular raster-based solutions. Attempts to introduce TIN-mesh into operational hydrology are done by, for example, Ivanov et al. (2004) with a case study performed on three watersheds for seven years. The results were promising, though the authors noted that the model itself was not used operationally. With the introduction of the Mesher tool (Marsh et al., 2018), advances dedicated to hydrologic simulations are achieved, enabling the creation of triangular irregular meshes. While for physically-based models it has been shown that accounting for terrain structures bring direct benefit, helping to explain and simulate events precisely, the application has generally been limited to research-based modeling. The advantages for operational hydrology are still to be assessed, and must take into account factors related to the complexity of implementation, availability of data sources and code.

The main objective of the present study is to introduce toolbox for hydrologic simulations on irregular triangular networks (TINs). First, we test sensitivity of Shyft.hydrology (Burkhart et al., 2021) simulations to mesh size and shape. Secondly, we

present new radiation routines for Shyft.hydrology, which allow "on the fly" correction of incoming solar radiation (S) based on underlying topography. Shyft.hydrology is a part of Shyft open-source toolbox, actively used and supported by Statkraft, that contains the operational tools for distributed hydrologic modeling. The new part of the software allows detailed capture of terrain topography and simulates slope and aspect effects. The TIN mesh is created using Rasputin meshing tool, also introduced herein. The slope and aspect of each TIN is directly impacting radiation flux of Shyft, which is modeled based on routine proposed by Allen et al. (2006). The proposed toolchain allows to study impact of hillslope variations in incoming solar radiation on important variables within hydrology domain. Particularly, we show that at the catchment scale for snow-covered areas incorporating topographic effects impacts snow accumulation and melting processes as well as evapotranspiration.

The paper is structured the following way. Section 2 presents parts of the toolchain. In section 2.1 Rasputin tool is presented. We demonstrate basic functionality of Rasputin in section 2.1.1 and show mesh refinement example in section 2.1.2. Shyft.hydrology is presented in section 2.2, where we remind on PTGSK-stack presented in the Shyft model desciption paper (Burkhart et al., 2021) in section 2.2.1 and present new RPTGSK stack in section 2.2.2 with aforementioned radiation routine. We also talk briefly about shyft cells in section 2.2.3. Section 3 is dedicated to demonstration of functionality of proposed toolchain. We present area in section 3.1. Methods are outlined in section 3.2. Forcing dataset is presented in 3.3. Performance metrics is briefly discussed in 3.4. We talk about TINs impact on interpolation of precipitation and temperature in **??**, sensitivity of discharge to mesh shape is shown in **??**. We analyse sensitivity of shyft simulation to TIN mesh resolution in **??**. Section 3.6 is dedicated to demonstration of possibilities coming from incorporating "on the fly" correction of incoming solar radiation for simulations. We perform virtual rotations of underlying cells. In 3.6.1 we show interpolation and slope/aspect correction of incoming solar radiation. We calibrate the model and analyse water balance components in 3.6.2. Section **??** briefly describe recent application of the toolchain for detailed hydrological analysis of Marsyangdi-2 subcatchment (CID-8) in Central Nepal, Himalaya. In section 4 we provide discussions on difficulties met in the study and limitations, that could be a focus of future research. Section 5 provides concluding remarks.

2 Toolchain components

2.1 Rasputin Meshing Tool

2.1.1 Basic functionality

The Rasputin software https://github.com/expertanalytics/rasputin converts point set of (x, y, z) coordinates into triangulated irregular network (TIN). The main usage is conversion of raster DEMs into simplified triangular meshes. The tool is freely available under GNU GPLv.3 lisence and combines C++-code for efficient computations and Python interfaces for ease of use. It is based on several well-known and tested software packages: CGAL (https://www.cgal.org) – for triangulation and simplification routines, pybind11 (Jakob et al., 2017) – to generate Python wrappers; Pillow ((https://python-pillow.org)) to read GeoTIFF (https://en.wikipedia.org/wiki/GeoTIFF) files; Meshio to write results, https://github.com/nschloe/meshio, (Schlömer et al., 2020); and Armadillo for speedy arithmetics, http://arma.sourceforge.net (Sanderson and Curtin, 2016), (Sanderson and

Curtin, 2018). The source code, details on each dependency and installation procedure are described at https://github.com/expertanalytics/rasputin.

The triangulation routine is based on the CGAL Delaunay method (https://doc.cgal.org/latest/Triangulation_2/index.html). Delaunay triangulation dates back to 1934, and there are plenty of available algorithms in computational geometry literature, some of them described in, for example, (Bowyer, 1981), (Tsai, 1993), (Devillers, 1999), (Boissonnat et al., 2009) and (Boissonnat et al., 2019). The CGAL software implements the *Incremental Randomized Delaunay Triangulation algorithm* (Devillers, 1999), (Kettner et al., 2008) with several design choices aimed for robustness and flexibility as described in Boissonnat et al. (2002). Some recent updates of the algorithms are presented in Devillers and Teillaud (2011) and Fogel and Teillaud (2013). A comparison done by Liu and Snoeyik (2005) demonstrate that decisions taken while implementing the Delaunay triangulation (3D example) impact the results of tessellation significantly and affect performance, with CGAL mentioned as one of the good options to work with. Rasputin utilizes non constrained 2D Delaunay triangulation.

Figure 1 demonstrates the results of mesh generation for Marsyangdi-2, CID-8 (the subcatchment is described in 3.1, fig. 5) visualized by the Rasputin internal visualization tool. As can be noticed with the coarsening grid the lake in the upper left corner of the area is almost lost, with only 2 representative triangles left. This is a result of the lack of land-type constraints. A subsequent revision of Rasputin will introduce this kind of constraint (this functionality is available in, for example Mesher (https://github.com/Chrismarsh/mesher) described in Marsh et al. (2018)), so the representative land types are assigned more accurately.

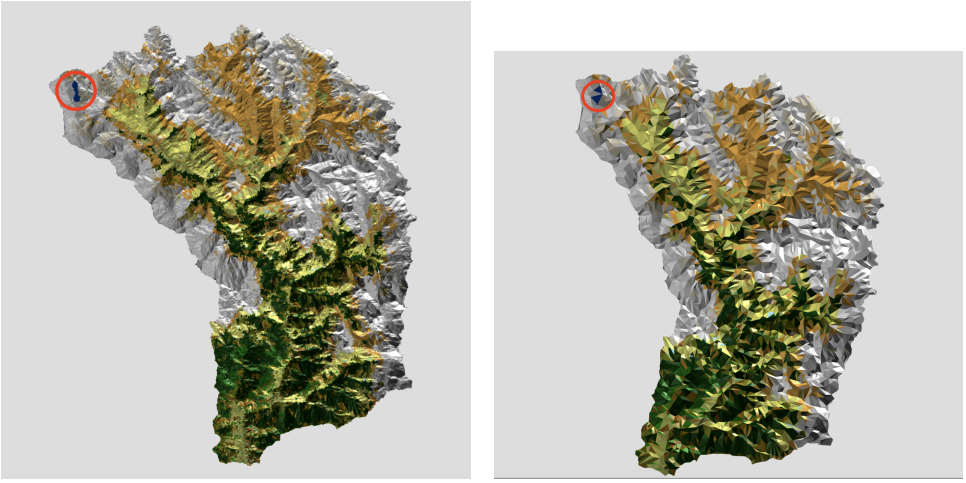

(a) (b)

Figure 1. Marsyangdi-2 subcatchment (CID-8) of Narayani river basin in Central Nepal. 3D-visualisation inside Rasputin: a) high resolution mesh with 74014 cells, b) low-relution mesh with 7310 cells

The half-edge collapse algorithm from CGAL based on Lindstrom and Turk (1998) and Lindstrom and Turk (1999) is used in Rasputin, which coarsens the mesh minimizing the deformations based on the given cost function. There are 2 options of cost function in Rasputin: a) the target ratio for edges in the result mesh to edges in initial mesh and b) maximum number of

edges in the result mesh. With both options of the cost functions, the algorithm coarsens the TIN-mesh in a way, that TINs in flat areas are merged first, and only after that the peaks of mountains are coarsened. Simple visual demonstration of hillslopes smoothing is demonstrated on the fig. 2. The figure shows height distributions: the left column for a fine-resolution mesh (74014 cells) and the right column for a low-resolution mesh (7310 cells), and a simple visual explanation of the coarsening done for this example: the red line shows the resultant coarse mountain.

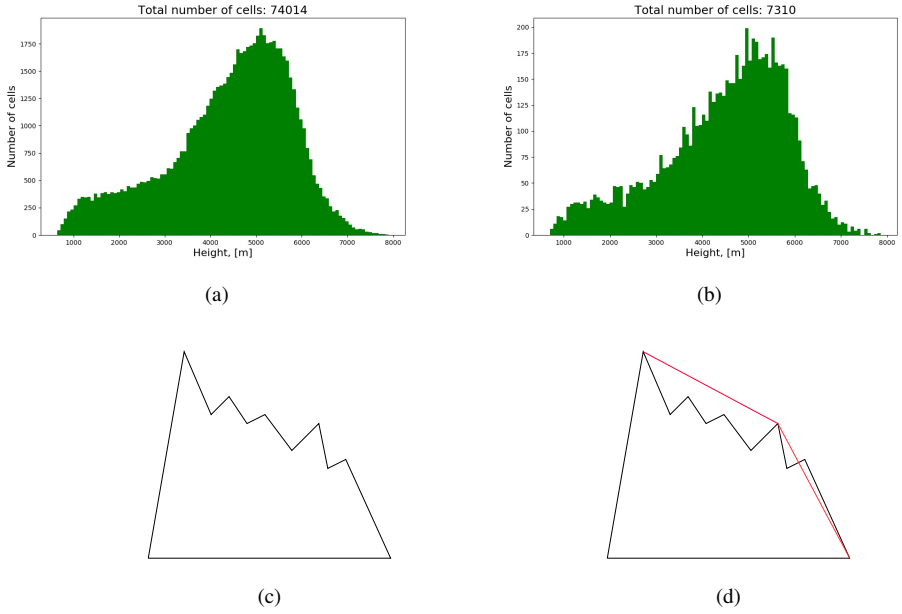

Figure 2. Elevation distributions Marsyangdi-2 subcatchment (CID-8): a) high resolution (74014 cells), and b) low resolution (7310 cells). Simple visual explanation of hillslope coarsening: c) high resolution mesh keeps all details of topography, d) low resolution mesh keeps highest peaks, while lower ones in between are smoothed by the algorithm.

The land types are assigned to each TIN based on the middle point position in the GlobCov 2009 (http://due.esrin.esa.int/page_globcover.php) or Corine (Europe) (https://land.copernicus.eu/global/products/) datasets with resolutions 300m and 80m respectively. In the appendix A fig. A1 TINs for two landtype sources are shown. Corine is much more accurate for the particular area in Norway. An equivalent high-resolution land type map in Nepal was not available, so GlobCov was used.

The recent versions of Rasputin generate TIN-mesh in xdmf-format (https://en.wikipedia.org/wiki/XDMF), so the mesh can be exported into numerous visualisation and/or simulation tools, including ParaView (https://en.wikipedia.org/wiki/ParaView).

2.1.2 Example of mesh refinement

We explore further meshes and TIN generation methods for subcatchment 10 of the Narayani river basin (Budhi-Gandaki, CID-10 on the fig. 5). Our goal is to visually asses the quality of the underlying topography representation before conducting any hydrological experiment. For the purpose of the experiments we have developed three grids: i) a regular grid which contains

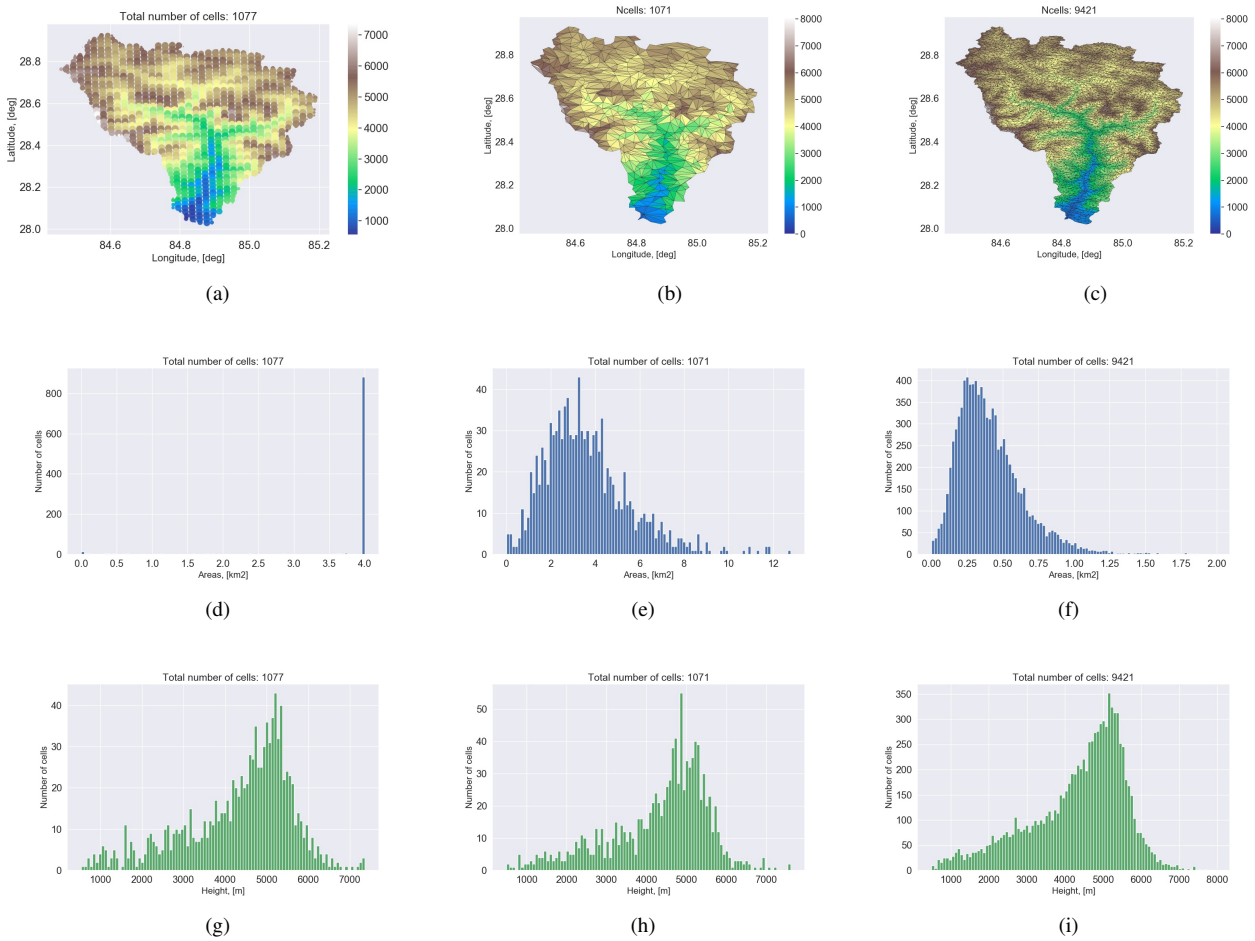

Figure 3. Scatter plot for the regular grid and contour plots for TIN-meshes with areas and heights distribution : left column (a), d), g)): classic/regular grid, middle column (b), e), h)): tin-ocs mesh, right column (c), f), i)): tin-slr mesh

1077 "cells", ii) a low resolution TIN, which we term "tin-ocs" containing 1071 "cells", and iii) a high resolution TIN, referred to as "tin-slr" containing 9421 "cells" (see Table 1). We also present statistics for higher resolution meshes: "tin-lr" with 47558 cells and "tin-mr" with 478638 cells, which were used for simulations in subsection **??** among other meshes, not shown in this section.

Figure 3a) shows scatter plot generated from a regular grid. This type of grid was used, for example, in Bhattarai et al. (2020a). The cells are a regular grid with 2 km x 2 km. The scatter point size is taken based on each cell area in km^2. The cells less than 4 km^2 are result of the polygon clip process, which is described in Burkhart et al. (2021). Figure 3b) and c) show TIN-meshes. The triangulation procedure in Rasputin generates triangles of different sizes: the flatter the area, the bigger triangles are generated (see, also app. A fig. A1, where water bodies have larger cells compared to the terrain around).

The highest possible resolution for the underlying DEM generates 958144 cells (not presented here). It is important to notice that the catchment boundaries are treated more carefully with increasing resolution. As expected, the finer the mesh, the more precise the catchment area, also more topographic details can be captured. However, we show further that representative for particular simulation features may be captured without the extreme case of the highest resolution.

The effective area (the effective catchment area for the TIN-mesh is calculated as a sum of areas of cells projected on the horizontal plane) (fig. 3d),e),f)) and elevation distributions (fig. 3g),h),i)) for generated meshes show some interesting features. When comparing classic/regular grid with TIN-mesh with almost same number of cells (tin-ocs): the distribution of areas is much greater, with many of large and small cells. This difference has a direct impact to the subsequent distribution of forcing variables (showed in sec. 3.6). Table 1 shows statistics for the compared meshes. The median of TIN-mesh with almost same number of cells is 18% lower, and there are only a few smaller cells (only to characterize the borders) in the regular grid. The increase in cell number for TINs leads to regular triangular grid with cell areas 0.004 km^2, where size is limited by raster resolution. One can notice that Rasputin mesh and regular cells with the same amount of cells have a differences in the elevation distribution: the median height for all TIN-meshes is generally lower. This is an interesting outcome, as many procedures considering elevations (for example, interpolation of temperatures) will be impacted by this variation.

The TIN-mesh also carries enough information for the user to calculate slope and aspect for each cells center point. Averaged values across the whole subcatchment are shown in Table 1, with slope being more than 30°.

Table 1. Geometry statistics for meshes used in experiments

	Regular grid	TIN-ocs	TIN-slr	TIN-lr[a]	TIN-mr[a]
rasputin ratio[b]	–	0.00117	0.01	0.1	0.5
Ncells	1077	1073	9421	47558	478638
Mean real area, [km^2]	3.59	4.26	0.51	0.10	0.01
Mean effective[c] area, [km^2]	3.59	3.62	0.41	0.081	0.0081
Median area, [km^2]	4.0	3.30	0.37	0.073	0.007
Mean cell height, [m]	4348.2	4327.8	4331.97	4284.8	4263.06
Median height, [m]	4673.90	4664.04	4647.84	4595.32	4577.40
Average cell slope, [deg]	0.0	30.86	34.56	34.54	33.19
Average cell aspect, [deg]	0.0	183.23	180.31	180.91	181.0

[a] This mesh was used in experiment presented in subsection **??**

[b] *Rasputin ration* 1.0 generates 958144 cells with mean effective area of 0.004 km^2, parameter controls mesh generation

[c] *Effective area* is an area of a triangle projected on the horizontal surface

2.2 Shyft Hydrologic Framework

Shyft (https://gitlab.com/shyft-os/shyft) contains a complete suite of tools for conceptual hydrologic simulation in hydropower production industry, and is particularly useful for regions with complex topography or data sparse regions owing to the hybrid nature of physically based and conceptually implemented algorithms. From it's first versions (Burkhart et al., 2016) to recent state (Burkhart et al., 2021), shyft has developed into valuable tool for operational hydrology.

This study introduces a new approach in Shyft, which allows the usage of triangular cells with all the geometrical characteristics like normal, slope, aspect, real and effective areas, so that connecting to Rasputin (or most any other software, which can generate TIN vertices) is achieved via a simple parsing procedure in the Python repositories. Burkhart et al. (2021) provide a more detailed description of the framework, however, for completeness, here we briefly describe the main components used in this study.

The hydrologic model provides a set of methods (*model stack*) describing the complete rainfall-runoff model for each cell. Cells are linked via catchment definitions and simple routing procedures. We conduct a series of experiments using regularly gridded cells and newly introduced TIN, which creates an irregular triangular mesh of cells. Each cell is using the PTGSK and RPTGSK model stacks.

2.2.1 PTGSK-stack

The existing PTGSK stack contains the following methods:

- PT – Priestley-Taylor method for estimating potential evapotranspiration (Priestley and Taylor, 1972),
- GS – gamma-snow method: the energy balance routine for snow accumulation, snow melt and subgrid snow distribution described in Hegdahl et al. (2016) ;
- K – catchment response function developed by Kirchner (2009);

Forcings: precipitation $P, [mm/h]$, temperature $T, [^0C]$, real humidity $RH, [-]$, wind speed $WS, [m/s]$, short-wave radiation $S, [watt/m^2]$ are interpolated and fed to the *model stack*, which is briefly described in app. B.

2.2.2 RPTGSK-stack

The RPTGSK stack is based on the PTGSK, but the radiation method is added to apply slope and aspect correction of radiation input based on the procedure described in Allen et al. (2006). The results of algorithm verification and sensitivity study are available as part of Shyft documentation (https://gitlab.com/shyft-os/shyft-doc/tree/master/notebooks/radiation). Although, the algorithm from Allen et al. (2006) calculates also theoretical clear-sky radiation, the following description of S correction is based on eq. (38) from the paper, which "translates" solar radiation measured on the horizontal surface (R_{sm} in the paper) onto

inclined surfaces. S is a function of the R_{sm}, topography and air conditions related to clearness and transmissivity:

$$\begin{aligned} S &= R_{sm} \cdot \left(f_b \frac{K_{B_{hor}}}{\tau_{sw_{hor}}} + f_{ia} \frac{K_{D_{hor}}}{\tau_{swhor}} + \alpha(1 - f_i) \right) \\ &= R_{sm} \cdot f(latitude, aspect, slope, elevation, T, RH, \alpha, K_t, day\_of\_the\_year), \end{aligned} \tag{1}$$

where f_b is the ratio of expected direct beam radiation on the slope to direct beam radiation on the horizontal surface, K_{Bhor} the transmissivity index for actual direct beam radiation on the horizontal surface, K_{Dhor} the index for actual diffuse radiation on the horizontal surface, and $\tau_{sw_{hor}}$ is the actual atmospheric transmissivity (direct + diffuse) for the horizontal surface, f_{ia}, f_i are factors related to anisotropic or isotropic diffuse radiation, α the average albedo of the surrounding ground below the inclined surface, K_t is an empirical turbidity coefficient $0 < K_t < 1$, where $K_t = 1$ represents clean air and $K_t < 0.5$ is extreme dusty or polluted air. The ratios on the right side of eq. 1 are calculated from forcings and topography coming from the mesh.

According to the analysis conducted while developing routines, the radiation outcome of eq.1, which is taken from Allen et al. (2006) eq. (38), is mostly impacted by latitude, aspect and slope. Figure 4 shows impact of slope and aspect on the translated radiation, using station 06191500 "Yellowstone River at Corwin Springs MT" data from Camels dataset (Newman et al., 2014; Addor et al., 2017). The rest of the inputs to the routine (elevation, temperature, relative humidity, albedo, turbidity) are mainly used in calculation of theoretical clear-sky radiation output, with albedo and turbidity, related to clearnsess and transmissivity being the most significant ones. Detailed analysis of the routine is presented in https://gitlab.com/shyft-os/shyft-doc/tree/master/notebooks/radiation.

2.2.3 Monocell vs fractional cell types

In Shyft a cell is essentially a geo-located area, on which the model stack is applied. In the classic application with regular grid cells, a fractional description of land cover is used, meaning that it was possible to have a 50% of cell covered by *forest*, 20% by *glacier* and the rest left *unspecified*. The common semi-distributed approach in many large-scale models like VIC (Liang et al., 1994), allows group response units (GRU) and hydrological units (HRU), combining similar hydrologic or terrain features together. The HRU can contain number of large, flat grid cells, each with “tiles”, corresponding to the fraction of the cell covered by the particular land cover. Weighted averages of fluxes and storages from the tiles give grid-cell average values. Though, Shyft allows this approach for grid-based simulations, for the tin-based simulations we decided to move to the concept of a *monocell* type. Thus, to each TIN-cell only one land type is assigned, where information on each triangle comes directly from Rasputin mesh, which is similar to the approach used in Marsh et al. (2020). This greatly improves the ability to distinguish different land types accurately. However, the current state of the software describes only several internal types of land cover: *lake*, *reservoir*, *forest*, *glacier* and *unspecified* area. So the land cover produced by Rasputin is mapped onto these 5 internal types. This is a result of initial simplicity of the Shyft concepts. Further development of more physically based methods (for example, steps are taken to introduce Penman-Monteith evapotranspiration, see https://gitlab.com/shyft-os/shyft-doc/tree/master/notebooks/penman-monteith) requires specifying more internal types, so mapping of land cover coming from Rasputin to Shyft will be more accurate moving forward.

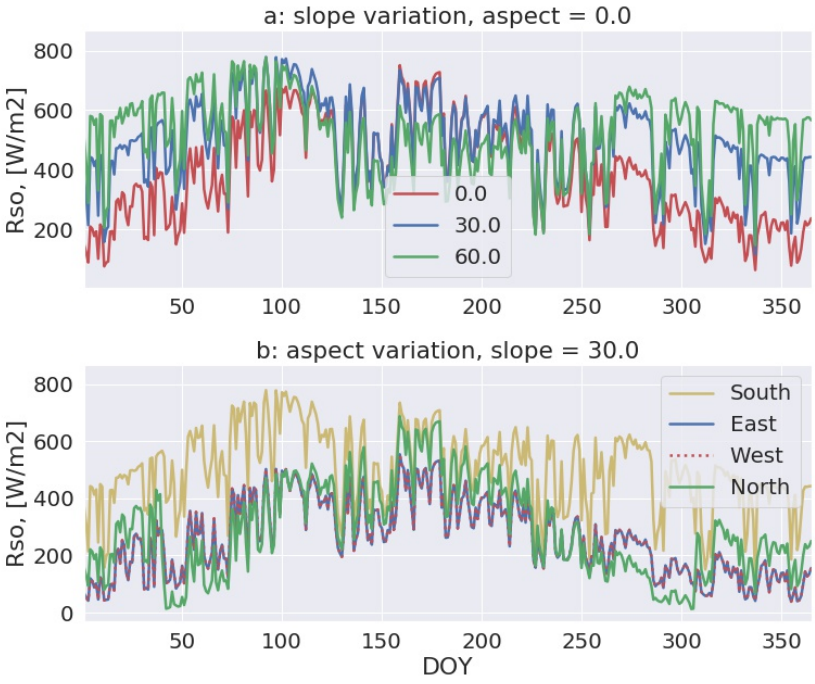

Figure 4. Impact of topographic features variations on resultant corrected S for Camels 06191500 station data, year 1980: a) slope variation with fixed aspect, b: aspect variation with fixed slope.

3 Functionality demonstration

In this section we present "proof of concept" experiments with Shyft and Rasputin toolchain applied for the catchment in central Himalaya. The Himalaya region is known to have extreme topographic variability, with sparse observational networks. Additionally, commonly used meteorological forcing datasets have coarse grids. The area was selected as it provides a good option to demonstrate the potential application and assess the benefits of TIN-meshes on a region with significant topographic structures as well as significance for water resource management. In addition, the region is prone to global warming, which might affect millions of people dependent on the water coming from the upstreams. The hydrologic importance of changes in timing or amount of snowmelt in the region was shown by Bookhagen and Burbank (2010).

3.1 Study area

The Narayani river basin shown on the fig. 5 is located in central Nepal and China (around 13% of the area). Originating at the southern edge of Tibetan Plateu, the river flows through Nepal to reach Ganges in India. The main gauging station is operated by the Department of Hydrology and Meteorology, Government of Nepal (DHM, GoN) and located in Narayanghat

(27° 42′ 30″N 84° 25′ 50″E). According to Omani et al. (2017) 8% of area is covered by glaciers. The catchment area is 31692 km^2 with elevations ranging from 175 m.a.s.l in the south to 8148 m.a.s.l in the north. Hydroclimatic regime of the region is defined by seasonal weather variations with pre-monsoon period (March to May), monsoon (June to September), post-monsoon (October to November) and winter (December to February). The majority of total precipitation (80% according to Kripalani et al. (1996)) occurs during monsoon.

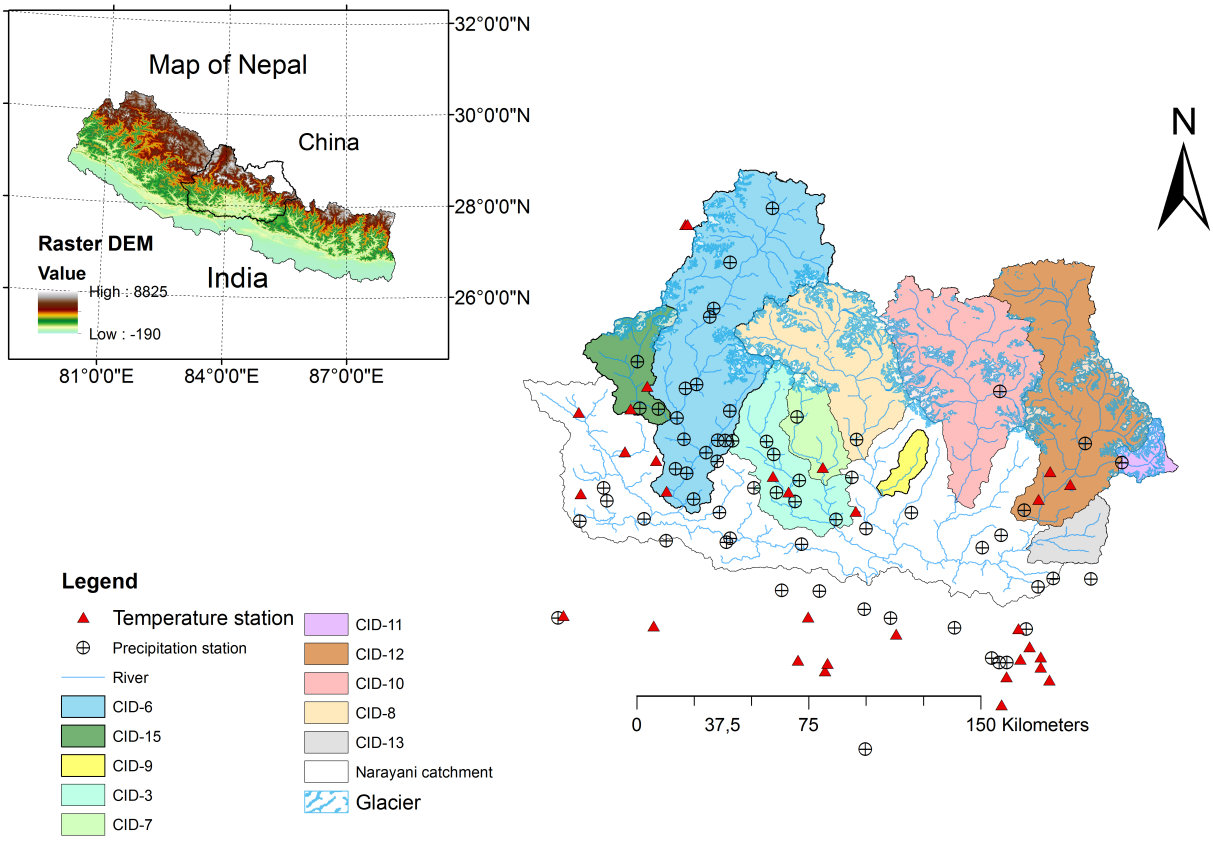

Figure 5. Narayani river catchment with subcatchments used in the demonstration: CID-3-7 (Seti Gandaki), CID-8 (Marsyangdi-2), CID-9 (Chepe Khola), CID-10 (Budhi-Gandaki), CID-11-12 (Betrawati), CID-13 (Tadi Khola), CID-15 (Myagdi Khola), CID-6-15 (Kali-Gandaki)

On the figure 5 subcatchments used in the study are shown in various colors. When talking about subcatchments, we either use "subcatchment" with number, or "CID-" and number, where CID reads as catchment with ID. Based on the average height three of the subcatchments (CID-3-7 (Seti Gandaki), CID-9 (Chepe Khola), CID-13(Tadi Khola)) are considered low-land (average height $\leq$ 3000 m), the rest five (CID-8 (Marsyangdi-2), CID-10 (Budhi-Gandaki), CID-11-12 (Betrawati), CID-15 (Myagdi Khola), CID-6-15 (Kali-Gandaki)) are high-land. Subcatchments CID-9, CID-13 and CID-15 are relatively small (area $\leq$ 2000 km^2), and CID-6-15 is the biggest one, combining CID-6 and CID-15. In table 3 average areas and heights for

each subcatchment are presented. All values are extracted directly from a DEM. If the information is extracted from TIN or grid the average statistics vary based on resolution, which is shown in Table 1, so we consider information from raster as the most accurate.

Table 2. Subcatchments average area and height

	Low land			High land				
	CID-3-7	CID-9	CID-13	CID-8	CID-10	CID-11-12	CID-15	CD-6-15
Area, [km^2]	2690	302.3	650.8	3001.3	3867.0	4628.2	1079.23	7108.73
Height, [m]	1715.9	1845.4	1650.8	4377.2	4265.5	4349.5	3374.1	3780.4

Subcatchment 10 (Budhi Gandaki) of the Narayani catchment originates in China and extends to Nepal. The majority of the catchment lies in the Gorkha district of Nepal. CID-10 has an area 3867 km^2, which is partly covered by snow and glacier. The elevation within the catchment varies from 479 m.a.s.l at the Arughat hydrological station in the south to the Mount Manaslu of 8163 m.a.s.l in the north. The lowest debris-covered glacier lies at 3282 m.a.s.l. (Bajracharya et al., 2014). The mean annual precipitation in the subcatchment is 1800 mm with high spatial variability. We use this subcatchment as a main demonstration catchment with significant topographic variability. The catchment is also a subject to hydropower development with installed capacity of 1200 MW with average energy generation of 3383 GWh. (Budhigandaki Hydroelectric Project Development Commitee (BHPDC), 2015; Bhuju et al., 2016).

A Digital Elevation Model (DEM) of 90 meters spatial resolution is generated for the Narayani River basin using data from the Shuttle Radar Topography Mission (SRTM). SRTM DEMs are freely available for download from https://eros.usgs.gov/. The Qgis-software (https://www.qgis.org/en/site/) is used for automatic catchment delineation. Delineated catchments and the precipitation and temperature stations for the region are shown on fig. 5. Python scripts are prepared to convert shapely files to wkt-files, which describe polygons for input to Rasputin.

Table 3. Subcatchments average area and height

	Low land			High land				
	CID-3-7	CID-9	CID-13	CID-8	CID-10	CID-11-12	CID-15	CD-6-15
Area, [km^2]	2690	302.3	650.8	3001.3	3867.0	4628.2	1079.23	7108.73
Height, [m]	1715.9	1845.4	1650.8	4377.2	4265.5	4349.5	3374.1	3780.4

3.2 Methods

We conduct several experiments with PTGSK stack to study sensitivity of discharge simulation to mesh size and shape. In this **experiment set A** we manipulate cells sizes and shapes. The change in geometry is impacting the land type fractions as well as the interpolation of the forcing variables, which we demonstrate using CID-10 (Budhi Gandaki) in **exp. A1** and **exp. A2**. We provide comparison between triangular and regular types of meshes. Subcatchments CID-3-7, CID-8, CID-9, CID-10, CID-

11-12, CID-13, CID-15, CID-6-15 are used to study sensitivity to TIN-mesh resolution on the quality of discharge simulation, which is done in **exp. A3**.

Experiment set B with newly developed RPTGSK stack incorporates radiation routine, which allows correcting of incoming solar radiation based on slope and aspect of underlying surface cell. We make virtual rotation of underlying cells for CID-10 and demonstrate, how this type of manipulation propagate through model stack and outcome in a noticeable change in water balance components (SWE and evapotranspiration). Discharge is shown for only "normal" scenario and compared to PTGSK stack run on regular grid, as it was used as a calibration target for this experiment.

Experiment set C is showing the overall performance of TIN-based solution for discharge simulation at CID-10 (Budhi-Gandaki catchment). Discharge, evapotranspiration, snow-water equivalent and glacier melt are shown for 10 years starting from 2000-01-01, where either first or second half of the period was used for calibration, so second or first period was used for validation.

Table 4 presents the definition of experiments and expected outcomes.

Table 4. Experiments definitions

Exp. ID	Forcings	Subcatchment	Simulation details	Mesh	Outcome/Metrics
Experiments conducted with **PTGSK**-stack to analyze mesh resolution impact on performance of discharge simulation					
A.1	Observed: T and P, WFDEI: RH, S, WS	10	1 year, calibration only	grid2x2, tin-ocs,tin-slr	Q using NSE, KGE
A.2	Observed: T, WFDEI: P, RH, S, WS	10	1 year, calibration only	grid2x2, tin-cos, tin-slr	Q using NSE, KGE
A.3	Observed: T, WFDEI: P, RH, S, WS	3-7, 6-15, 8, 9 , 10, 11-12, 13, 15	5 years of calibration 5 years of validation	14-17 tin meshes	Q using NSE, KGE
Experiments conducted with **RPTGSK**-stack to study slope* $*$ and aspect* $*$ impact on SWE, Q and PE*					
B.1	Observed: T, WFDEI: P, RH, S, WS	10	1 year of simulation	tin-ocs, tin-slr	R_s, SWE and PE slope=var, aspect = North
B.2	Observed: T, WFDEI: P, RH, S, WS	10	1 year of simulation	tin-ocs, tin-slr	R_s, SWE and PE slope=var,aspect = South
B.3	Observed: T, WFDEI: P, RH, S, WS	10	1 year of simulation	tin-ocs, tin-slr	R_s, SWE and PE aspect=var, slope= 30^0
B.4	Observed: T, WFDEI: P, RH, S, WS	10	1 year of simulation	tin-ocs, tin-slr	R_s, SWE, Q and PE slope,aspect from mesh
C	Observed: T, WFDEI: P, RH, S, WS	10	5 year of calibration 5 years of validation	tin-ocs, tin-slr grid	Q slope,aspect from mesh, NSE and logNSE metrics

* SWE – snow-water equivalent, PE – potential evapotranspiration

** On the figures we use sl for slope and asp for aspect

3.3 Meteorological Forcing and Observed River Discharge Data

Forcing variables required for the PTGSK and RPTGSK stacks are: air temperature (T), precipitation (P), relative humidity (RH), wind speed (WS), and shortwave incoming solar radiation (S). All simulations are conducted at a daily temporal resolution, as the higher temporal resolution for observed variables was not available at the time of experiments. All Shyft algorithms allow any valid timestep (minutes, hours, 3-hours etc). Based on the study by Bhattarai et al. (2020a) the hybrid dataset is used. The three variables RH, S and WS are taken from the WFDEI. Temperature is observed, and precipitation is either observed or from WFDEI with GPCC method (see, (Weedon et al., 2014) for details on WFDEI datasets). The datasets are available at https://zenodo.org/record/3567830. In Bhattarai et al. (2020a) the observed forcings were manually checked for data quality. Furthermore, stations with less than 10 years or missing more than 15% of observations were removed. Therefore, only years 2000-2009 of observations met the requirements on data quality. The location and elevation of the stations is shown in app. D and as a supplementary material to Bhattarai et al. (2020a) . The stations are located below 4000 m.a.sl., which adds uncertainty to the study. As for the re-analysis data, the analysis performed previously showed that downscaled and bias-corrected ERA-I product (WFDEI) with the rainfall generated by Global Precipitation Climatology Center (GPCC) suits the best. The dataset has 0.5 x 0.5 degrees spatial resolution and daily temporal resolution. It is freely available at https://www.doi.org/10.5065/486N-8109. Discharge data for period 2000-2009 from the Department of Hydrology and Meteorology (DHM), Government of Nepal (GoN) is used for validation purposes.

3.4 Performance metrics

For defining quality of discharge simulation we use well known performance characteristics: Nash-Sutclife Efficiency (NSE) (Nash and Sutcliffe, 1970), Kling-Gupta Efficiency (KGE) (Gupta et al., 2009) and square root transformed Nash-Sutcliffe Efficiency (NSSQ) (Seiller et al., 2012). NSE, NSSQ, and KGE range between $-\infty$ to 1, where 1 indicates a perfect match. NSE is generally a measure best suited to show the predictive power during higher flow periods, while KGE is sometimes used to condition a model toward low flow periods. NSSQ shows general agreement of the simulated and observed discharge.

3.5 Experiments set A: Testing the sensitivity to mesh size of discharge for catchments in the Himalaya

We conduct **experiment A** for CID-3-7 (Seti Gandaki), CID-8 (Marsyangdi-2), CID-9 (Chepe Khola), CID-10 (Budhi-Gandaki), CID-11-12 (Betrawati), CID-13 (Tadi Khola), CID-15 (Myagdi Khola), CID-6-15 (Kali-Gandaki) with the forcing variables: observed temperature; WFDEI precipitation, incoming solar radiation, relative humidity and wind speed. The calibration period is 2000-01-01 – 2004-12-31, and the validation period is 2005-01-01 – 2009-12-31 at a daily timestep. The ranges for calibration parameters are shown in table C1, we will keep the ranges across whole set of experiments. Parameters on the right side of the column are set to constants, however, one can also set them for calibration. For further details on calibration values and their meaning, please refer to Burkhart et al. (2021) and https://gitlab.com/shyft-os/shyft-doc. The description of **PTGSK**-stack is also provided in Bhattarai et al. (2020a) and Bhattarai et al. (2020b). The catchment delineation is presented on the Figure 5. The main goal of this experiment is to draw a conclusion on what is the number of TIN-cells that can ade-

quately simulate runoff. So for each subcatchment we performed hydrologic simulations on 14 to 17 TIN-meshes with various resolutions.

Figure 6 demonstrates scatter plots of the NSE and KGE simulation results both for calibration (top row) and validation (bottom row) periods. In general, for all subcatchments meshes with $> 10^2$ cells perform satisfactory during calibration with $NSE > 0.55$ and $KGE > 0.6$. There is no further increase in efficiency with finer-mesh resolution. The performance of validation runs for subcatchments CID-9 and CID-15 is rather poor. This might be caused by incomplete and inaccurate discharge observations. The inaccuracy of CID-15 data might be averaged out, when looking onto CID-6-15. For the rest of the subcatchments performance during validation runs can be considered satisfactory with $NSE > 0.5$ and $KGE > 0.55$ for the $Ncells > 10^2$. From both calibration and simulation runs for $Ncells > 10^2$ there is no difference between small and large catchments and low-land and high-land catchments, all performing well, with the highest NSE and KGE found in CID-8 (high-land, medium size) and CID-13 (low-land, small size). However, we can see that for low-land subcatchmets (CID-13, CID-3-7) there seems to be no significant dependence of efficiency on the number of cells, with very small variations of NSE and KGE between various mesh resolutions. This is surely not the case for the CID-8, CID-10, CID-11-12, where the efficiency metrics decrease significantly for low-resolution meshes. The drop in efficiency for high-land subcatchments with low-number of cells supports the hypothesis that we miss some significant topography details when moving to lumped model. However, the initial simplicity of the Shyft routines does not allow us to improve results with increasing mesh resolution. Though, we see that for the terrain with low topographic variations even lumped models perform well, in order to conclude generally, we still have to study more catchments with higher variations in areas across the globe.

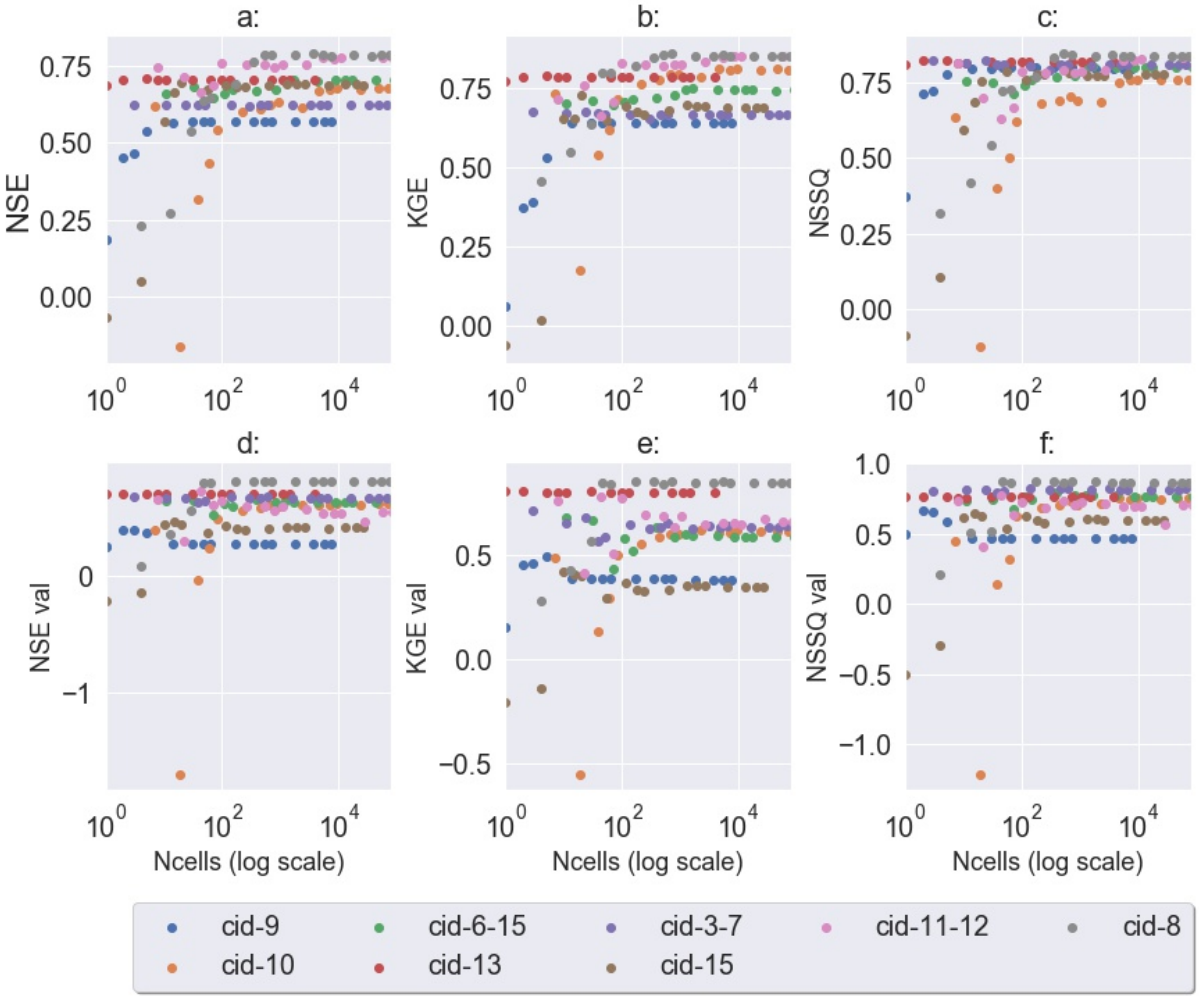

Figure 6. Top row: Scores for calibration period 2000-2005 a) NSE, b) KGE, c)NSSQ; Bottom row: Scores for validation period d) NSE, e) KGE, f) NSSQ

3.6 Experiment set B: Correcting incoming solar radiation "on the fly" for slope and aspect

Let us now analyze how accounting for slope and aspect will affect the incoming solar radiation and the snow simulation. We conduct a set of experiments on CID-10 with RPTGSK stack and 2 TIN-meshes, demonstrated in 2.1.2: tin-ocs (1071 cells) and tin-slr (9421 cells), with WFDEI P, RH, S and WS and observed T as forcing variables. The simulated year starts 1st of January 2000 (with 100 days of spin up period (from 23-09-1999)) at a daily timestep. Starting well before winter ensures that the snow model accumulates snow correctly. In this set of experiments we focus only on the demonstration, how different scenarios of correction of incoming solar radiation propagate through model stack. Thus, water balance components (SWE and E) are only shown for 1 year. **Experiment B.1** is performed with TIN-meshes, but all aspects of the TINs set to 0.0, meaning they look

North and only slope impact is studied. **Experiment B.2**: all the aspects of TIN-meshes are set to 180.0 (South). **Experiment B.3**: all slopes set to 31.0, so only aspects impact is studied. **Experiment B.4**: slopes and aspects are from real TIN-meshes. And we also simulate example with regular grid to perform comparison. The simulation run with regular grid is done with PTGSK stack (no radiation correction applied).

3.6.1 Interpolation of forcing: Incoming solar radiation

Let us look onto short-wave radiation interpolated onto the meshes. The interpolation method is IDW (inverse distance weighting) (Shepard, 1968) with same parameters for all meshes: maximum distance 600000.0 m, maximum members 10, distance measure factor 1.0. There is only one WFDEI cell covering the whole catchment, which ends up in rather homogeneous radiation. However, the maximum and minimum values of S after interpolation step for grid and TINs slightly differ, giving a) [187.89, 191.90], for grid b) [203.84, 207.64] for tin-ocs, and c) [203.79, 207.86] for tin-slr, and medians are a) 189.2, b) 205.1, c) 205.1 respectively. The difference is caused by the actually different positions of the mid-points of the cells.

Figure 7 shows the radiation translated onto inclined surfaces for the high-resolution TIN-mesh after applying slope-aspect correction algorithm. As one might expect based on previous studies, summarized in Fan et al. (2019), the topography impact is noticeable: the North-facing example clearly receives less radiation, compared to the South-facing experiment B.2. The impact of slope is also noticeable, as there is a visible difference between the slope-fixed radiation, fig. 7c) and the experiment B.4, fig. 7d), accounting for both slope and aspect variations. And overall difference in translated radiation compared to the initial interpolated values is huge. The minimum and maximum values for the 4 experiments are: a) [122.42, 209.0], b) [202.75, 263.17], c) [123.54, 258.62], d) [74.17, 263.71], and median values are: a) 151.03, b) 255.3, c) 150.56, d) 177.59. And the overall variation from cell to cell is well pronounced for all experiments, being far from the regular flat grid. Other important outcome is that the variations only in slope (exp.B1, and B.2 with aspect fixed) gives noticeable impact, increasing the range of values. The aspect impact studied in exp.B.3 seems to have the highest effect on the model. And the real mesh, where some cells might be north-facing or south-facing, or with other aspects, the range of radiation values is even higher.

Figures 8a,b) show values of radiation averaged over the whole subcatchment for the set of experiments on tin-ocs and tin-slr. As expected, the South facing experiment B.2 is having higher values compared to North-facing experiment B.1. The difference is especially noticeable during fall to spring period, which is consistent with the behavior of the model in the original paper by Allen et al. (2006). Both TIN-meshes show quite similar behavior between the experiments 1-4.

Figure 8c) shows averaged values for experiment B.4 for tin-ocs, tin-slr and also regular grid (which is obviously interpolated radiation). The curve representing coarse TIN-mesh is closer to the interpolated radiation, which is expected, as the slope and aspect values are much more inaccurate in that case. However, the results from both TIN-meshes are well below interpolated one, except for the December and January, when the model predicts higher values of incoming radiation.

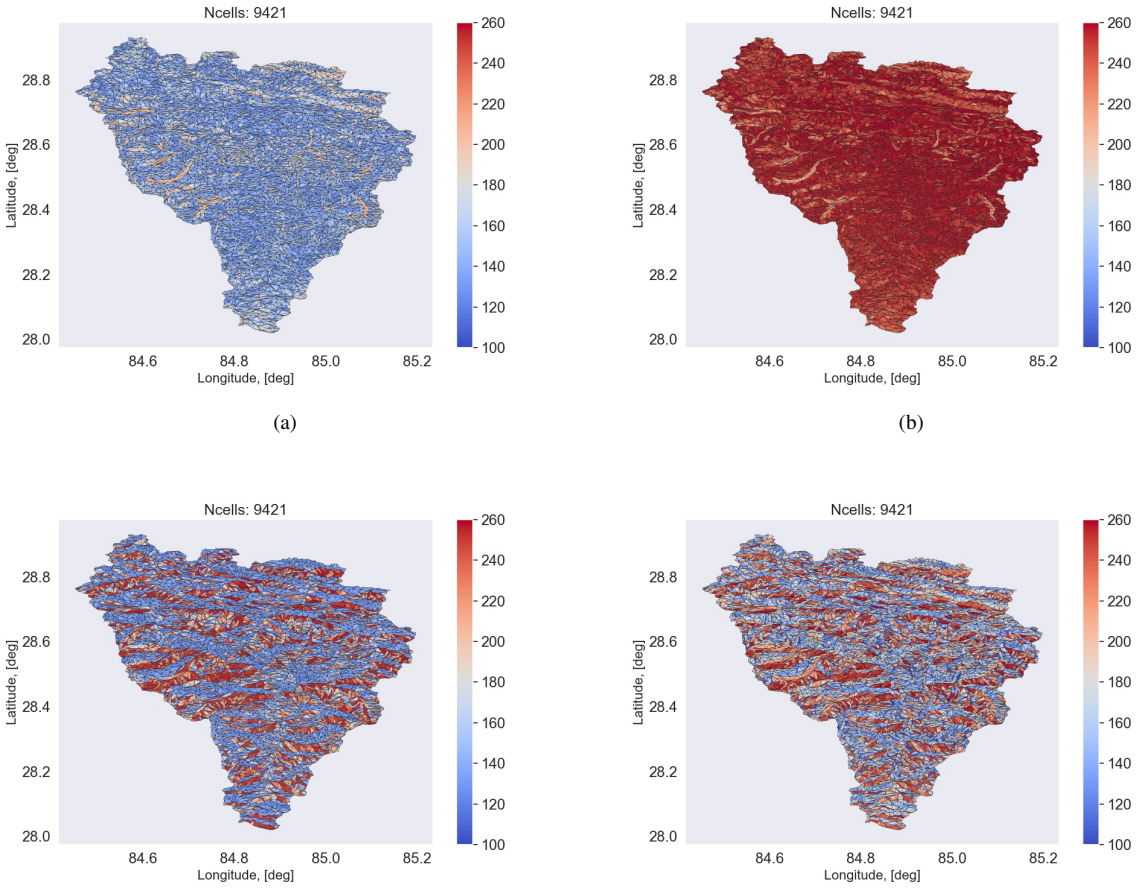

Figure 7. Experiments set B. Translated radiation, high resolution mesh: a) exp.B.1 (aspect = North), b) exp.B.2 (aspect = South), c) exp.B.3, slope=31.0, d) exp.B.4 (slope and aspect from TIN)

3.6.2 Simulated Water Balance Components

By now, we have already seen that slope and aspect variations of inclined surfaces impact the incoming radiation, being far from the one received by horizontal surfaces. As the radiation is a major component of surface energy balance, this change should propagate itself through the model stack to both snow simulation and evapotranspiration.

Simulated Snow-water equivalent

Figures 9a,b,c,d demonstrate SWE for the subcatchment derived from 4 experiments on tin-slr with table 5 summarizing some statistical difference. As might be expected: south facing example has lower averaged SWE compared to north-facing example. With the slope fixed to 31^0 (mesh mean slope) the amount of SWE differs from real situation. The variation is especially visible above 28.6^0 latitude, where average cell elevations are higher and more precipitation occurs as snow. The

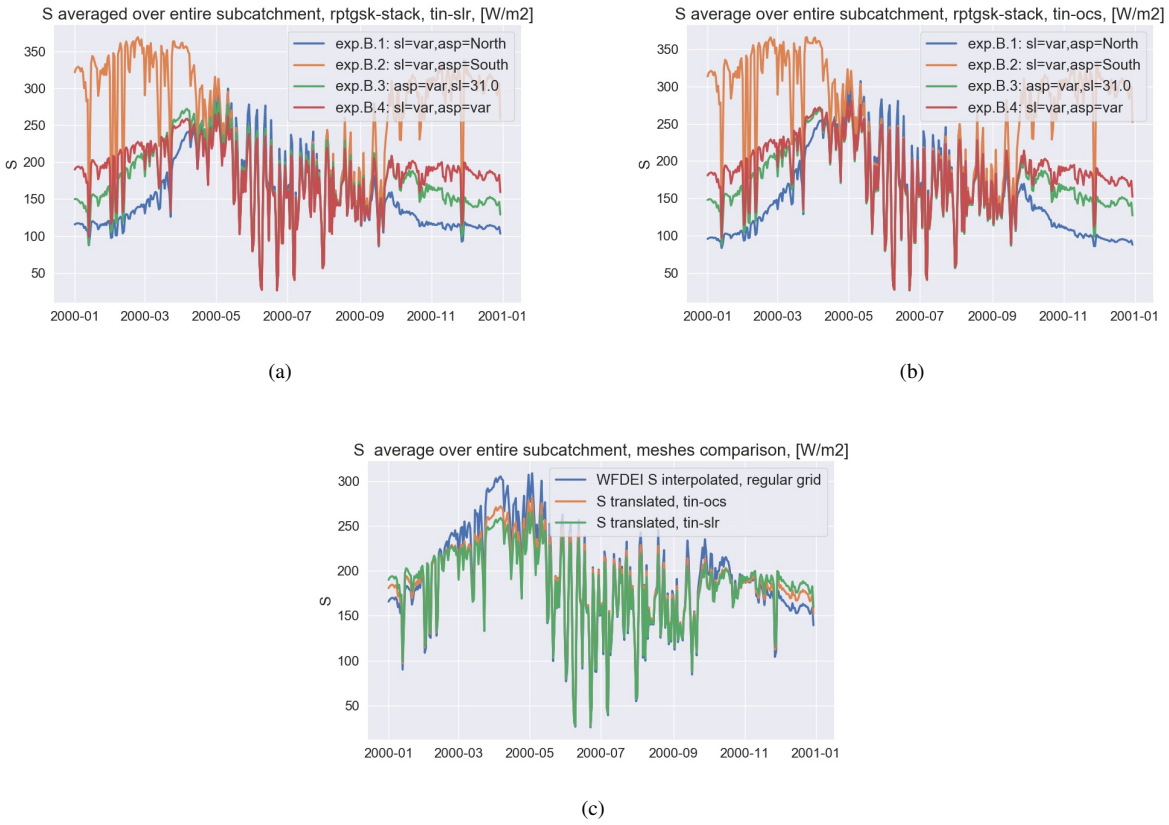

Figure 8. Experiments set B. Translated radiation averaged over the whole catchment: a) tin-slr, b) tin-ocs, c)comparison of slope/aspect tin-meshes ocs and slr with regular grid

maximum and minimum values are presented in table 5, with North-facing experiment B.1 having around 30% higher amount of snow compared to the south-facing exp.B.2. Experiment B.3 demonstrates that SWE is more sensitive to variation in aspect, which is also a result of higher range of radiation flux for the case. The experiment B.4 differs from the regular grid giving higher variation in SWE across the catchment, with increase in maximum value about 16% .

Table 5. Experiments set B, fine-mesh. SWE [mm] statistics

	B.1	B.2	B.3	B.4	Regular grid
min	0.0	0.0	0.0	0.0	0.0
max	169.29	122.45	146.65	156.8	130.38
mean	15.1	10.42	10.91	10.88	8.39
median	4.6	2.27	3.69	3.69	3.69

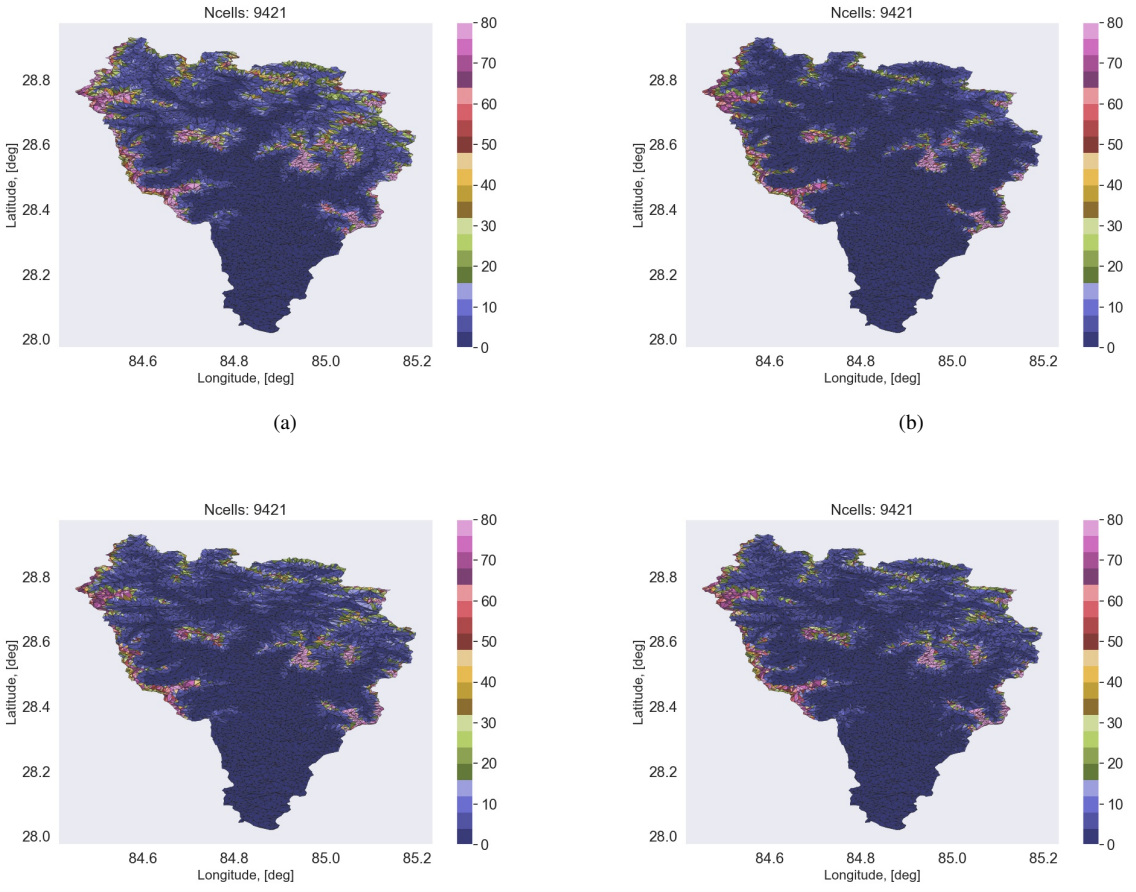

Figure 9. SWE with tin-slr: a) exp.B.1 (aspect = North), b) exp.B.2 (aspect = South), c) exp.B.3, slope=31.0, d) exp.B.4 (slope and aspect from tin)

The SWE area-averaged over the entire catchment is presented in Figure 10a) for the tin-slr and fig. 10b) for tin-ocs. The difference between 4 experiments is even more pronounced: the north-facing experiment results in higher SWE compared to south-facing one. The difference is more visible for the tin-ocs example, where the averaged value stays well below the 3 other experiments. For the tin-slr the south-facing example behaves in a different way form June to December being below the North-facing experiment B.1, but above the real mesh exp.B.4 and slope-fixed exp.B.3, dropping rapidly to lower values just at the end of December. Figure 10c) demonstrates comparison of experiment B.4 with tin-ocs, tin-slr and regular grid. As might be expected the tin-ocs is closer to the regular grid experiment. What is quite interesting is that the tin-ocs predicts higher SWE from the beginning of the year up to the monsoon starts and after that the tin-slr experiment gives around 13% higher values compared to the tin-ocs and 26% higher than regular grid.

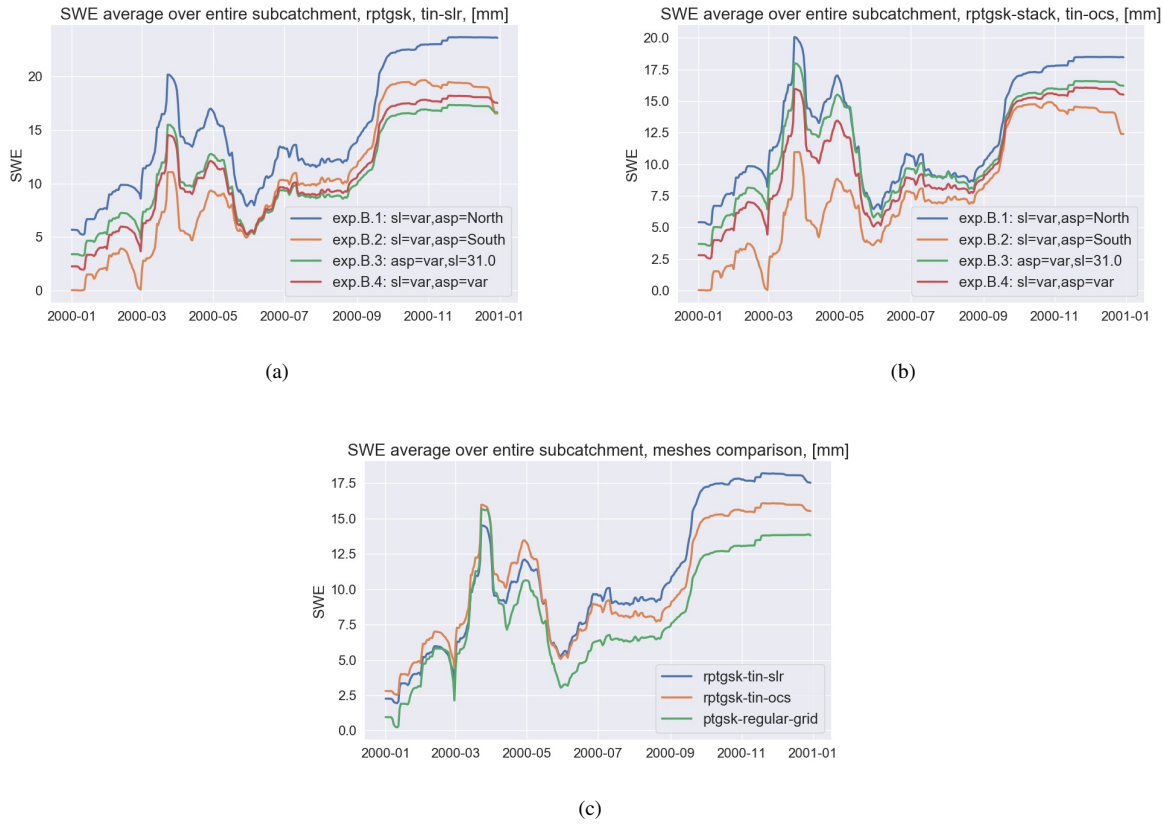

Figure 10. Experiment B. SWE averaged over the subcatchment: a) tin-slr, b) tin-ocs, c) comparison of real TIN-mesh of different resolutions with regular grid

Simulated Evapotranspiration

Figure 11 shows results for the potential evapotranspiration year-average for 4 experiments. As the radiation has direct impact onto the calculation of Priestley-Taylor evapotranspiration, the 4 experiments distinguish from each other clearly: south-facing experiment **B.2** evaporates more compared to the north-facing one **exp. B.1**.

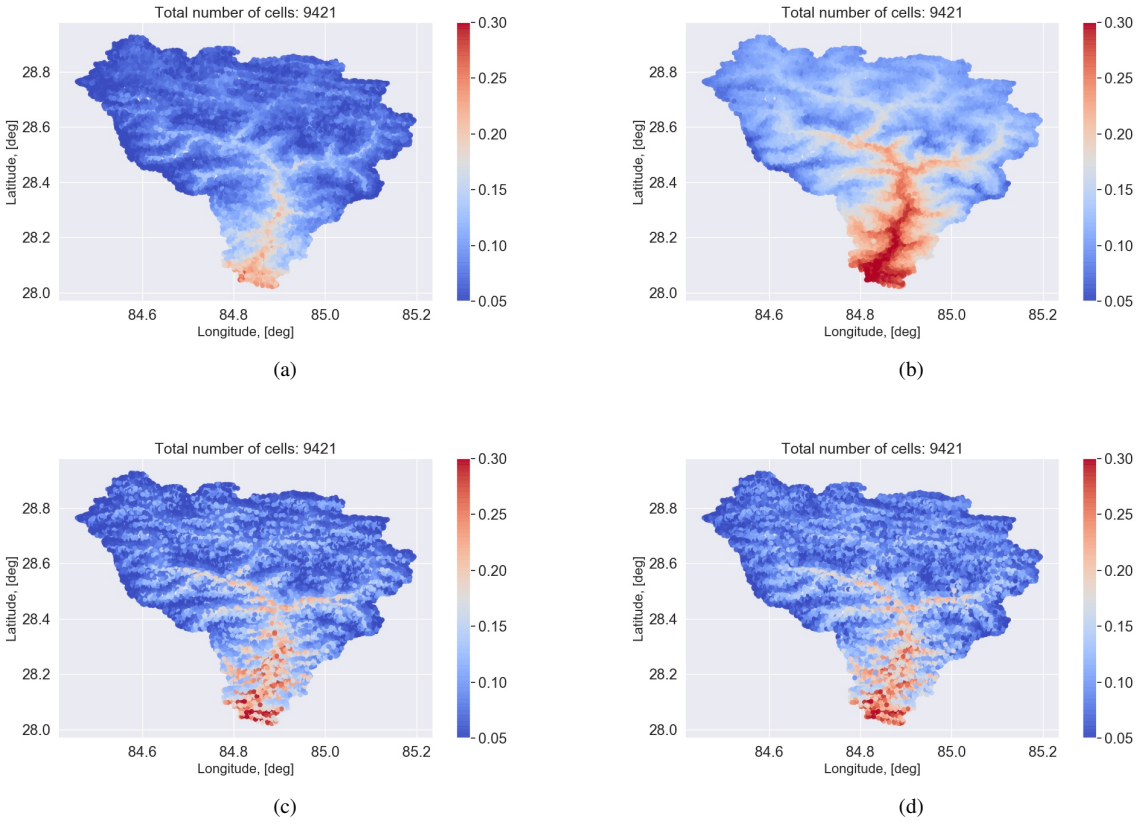

Figure 11. Potential evapotranspiration: a) exp.B.1 (aspect = North), b) exp.B.2 (aspect = South), c) exp.B.3, slope=31.0, d) exp.B.4 (slope and aspect from TIN)

3.7 Experiment set C: Testing sensitivity of Q to mesh size and shape, and slope/aspect correction for catchment in Himalaya.

In our previous study of CID-8 (Marsyangdi-2, Bhattarai et al. (2020b)) we showed that TIN-based model configurations outperformed grid-based model configurations for all validation years during 10 years simulation period from 2000-01-01, using WFDEI forcings. However, the results for CID-10 (Budhi-Gandaki) are not that straightforward.

3.7.1 Interpolation of temperature and precipitation

First of all we see, that there is a noticeable difference in interpolated temperature and precipitation. Figure 12 shows difference between values averaged across entire catchment for each day during the full period. Blue line correspond to the difference between tin-ocs and grid, orange line correspond to the difference between tin-slr and grid. The positive values mean that for both TIN meshes the average temperatures after interpolation step are higher compared to the grid. The temperature interpola-

tion method for all configurations is Bayseian temperature kriging with parameters: temperature gradient: -0.6 and temperature gradient standard deviation: 0.25, nuggget value for semivariogram : 0.5, range of semivariogram: 200000.0, sil value of semivariograml: 25.0 and height scaling factor: 20.0.

Figure 13 show difference between precipitation values averages across the catchment, where blue line correspond to the difference between tin-ocs and grid values, and orange line correspond to the difference between tin-slr and grid. Positive values mean that for the tin-slr the precipitation values are higher than for the grid, while for the tin-ocs the precipitation is lower with negative values on the figure.

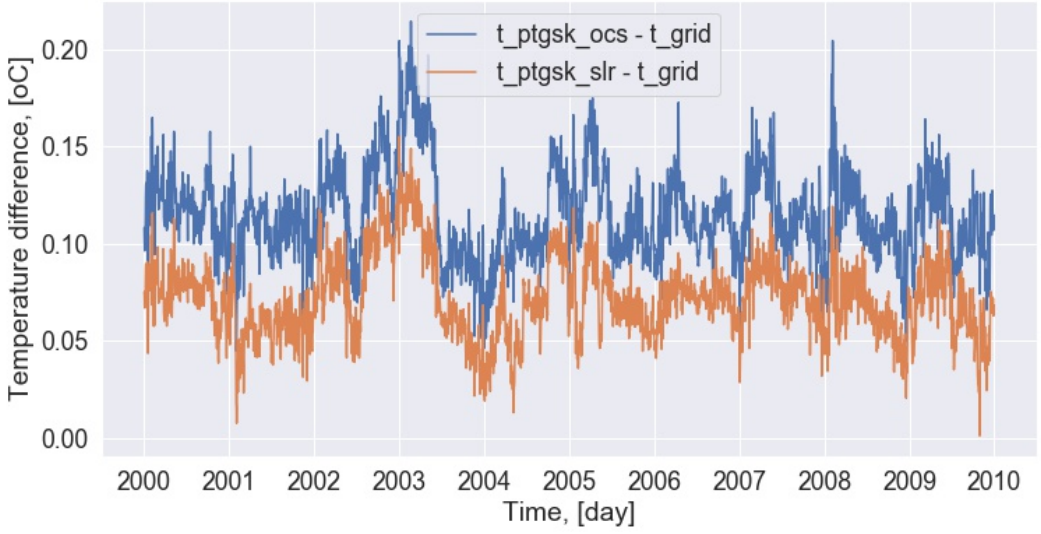

Figure 12. Experiments set C. Difference between interpolated temperatures averaged across the catchment

3.7.2 Hydrograph

We run simulation in two steps: a) calibration period is first 5 years from 2000-01-01 and validation period is second 5 years from 2005-01-01, b) vise versa, calibration from 2005-01-01 for 5 years and validation period 2000-01-01 – 2004-12-31. Figure 14 represent hydrograph of the measured and simulated discharge for validation periods and different model configurations. Some years show very good agreement between observed and modeled values in terms of NSE for all model configurations, while others agree poorly. Figure 15 demonstrate NSE and KGE scores for each model configuration for all validation years (two model runs). The TIN-based configurations (both PTGSK and RPTGSK) simulate particularly bad in terms of NSE the first period from 2000-01-01 til 2004-12-31. The second period from 2005-01-01 til 2009-12-31 correspond better between observed and modeled values for both NSE and KGE metrics in all model configurations. In general, grid-based solution demonstrate higher values of NSE and KGE for majority of the years. However, none of the configurations is able to

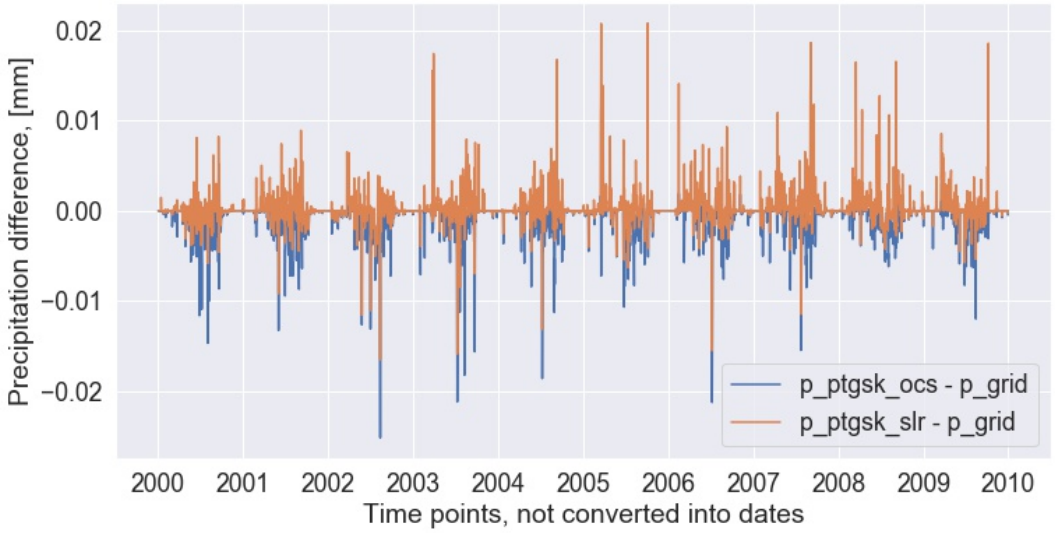

Figure 13. Experiments set C. Difference between interpolated precipitation averaged across the catchment

capture peak-flows during first period (2000-01-01 – 2004-12-31). The configurations with tins and RPTGSK stack perform slightly better than PTGSK-tin configurations, but still defeated by grid-based configuration.

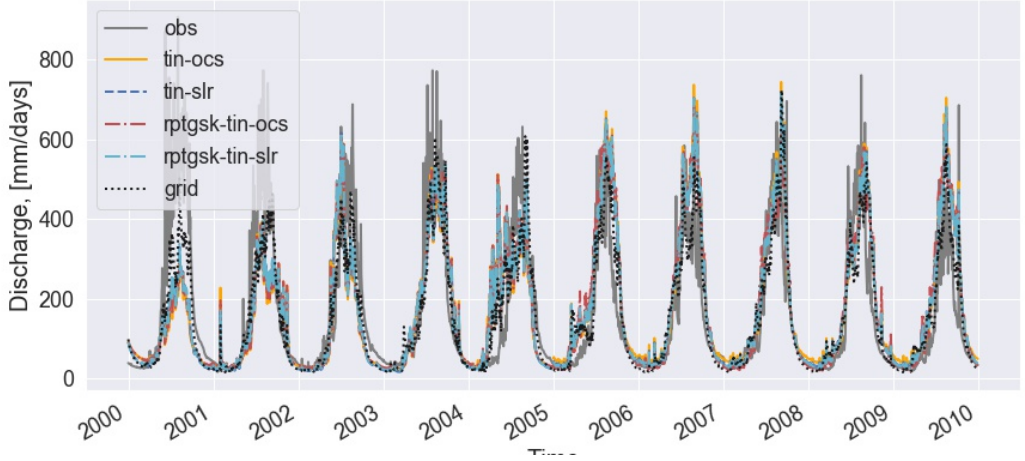

Figure 14. Experiments set C. Observed and simulated discharge for all model configurations.

This unexpected result motivated us to run the simulation once again, but using regional HI-AWARE datasset for P and T forcings. The HI-AWARE dataset has higher spatial resolution, but it requires more quality control. The results can't be

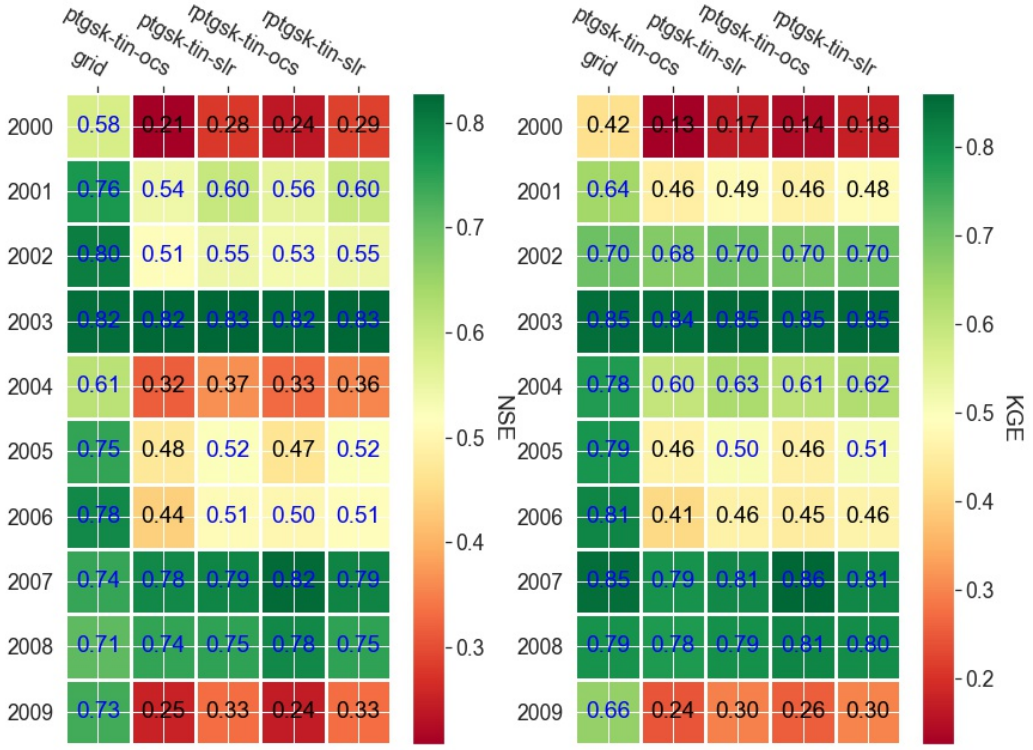

Figure 15. Experiments set C. NSE and KGE scores for different model configurations at each validation year.

interpreted clearly here, as, for example year 2009 (see, fig. 16) give very poor NSE nad KGE values. Other years, tend to vary between mesh types, resolution and stack configuration in a way, which is hard to draw any conclusion from. We attribute our findings to the fact that Budhi-Gandaki catchment has a very complex precipitation pattern, which the model was not able to capture properly, thus the results are so debatable.

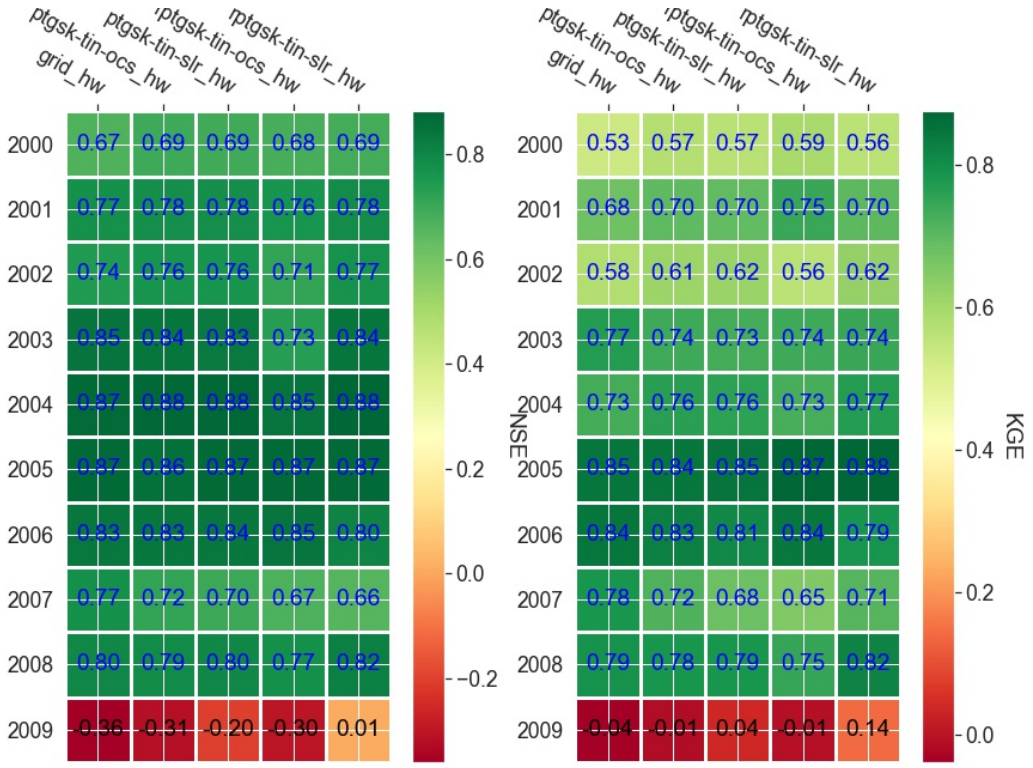

Figure 16. Experiments set C. NSE and KGE scores for different model configurations at each validation year with HI-AWARE P and T.

4 Discussion

4.1 Mesh resolution

Mesh resolution

In this research we analyze the impact of mesh-resolution on the efficiency of rainfall-runoff simulation in the Narayani river subcatchments. This region shows great variability in topography. We found that the initial simplicity of Shyft routines representing hydrology limits the possible improvements coming from high mesh resolution. Figure 6 clearly demonstrates that for each studied subcatchment there is a maximum number of cells, which is representative, and the number is relatively low. Actually, it turns out that figure 3b), which we initially considered rather coarse, is adequate representation of the CID-10 and the mesh fig. 1b) is more than enough to represent the CID-8.

Kirchner flexibility

In previous study by Teweldebrhan et al. (2018) showed that the most sensitive parameters for Shyft PTGSK stack are the kirchner c1, c2, c3 coefficients. We see that kirchner algorithm is very flexible. The initial idea of Kirchner (2009) was estimating parameters of the discharge to storage function $f = q(s)$. In Shyft we do not estimate this parameters, rather calibrate. So the function f, being at first a catchment feature tends to loose it's originality. And the results demonstrate that sometimes Kirchner routine actually gives a satisfactory efficiency value during calibration even with very low number of TIN-cells. Figure 17 shows Kirchner parameters for 3 subcatchments. The colors are same as were used in figure 6. There is very little variation in kirchner parameters for CID-13, which turns to be a rather flat one. As a result, we see that there is also very little variations in efficiency metrics. For CID-8, we see, that kirchner.c1 and kirchner.c2 parameters tend to reach some steady values, and this is highly correlated with the behavior of efficiency metrics with limit corresponding to the steady value. As for the CID-10, fluctuations in kirchner are correlated with greater variability in efficiency, and by the way, giving relatively high NSE for a very low number of cells. But still we see some kind of convergence. The efficiency parameters for this subcatchment are less satisfying than for 8 and 13, notifying us that there is actually no reason for more cells, as source data might be a greater issue. However, for CID-10 we found that grid-based solution perform better than TIN-based, which seems to be contradictory to our study (Bhattarai et al., 2020b) with CID-10, so additional investigations needed to understand such difference.

Land type constrains

Figure 1 reveals the importance of land type constrains, as without them, we might loose some essential information, when coarsening mesh. However, further analysis proves our initial hypothesis, that simplicity of Shyft is much greater limitation for the simulation, when lack of land type constrains. Other tools, like Mesher (https://github.com/Chrismarsh/mesher, described in Marsh et al. (2018) or ArcGis Pro (ESRI-ARCGIS, 2018) are valuable options to overcome the lack of land type constrains in triangulation.

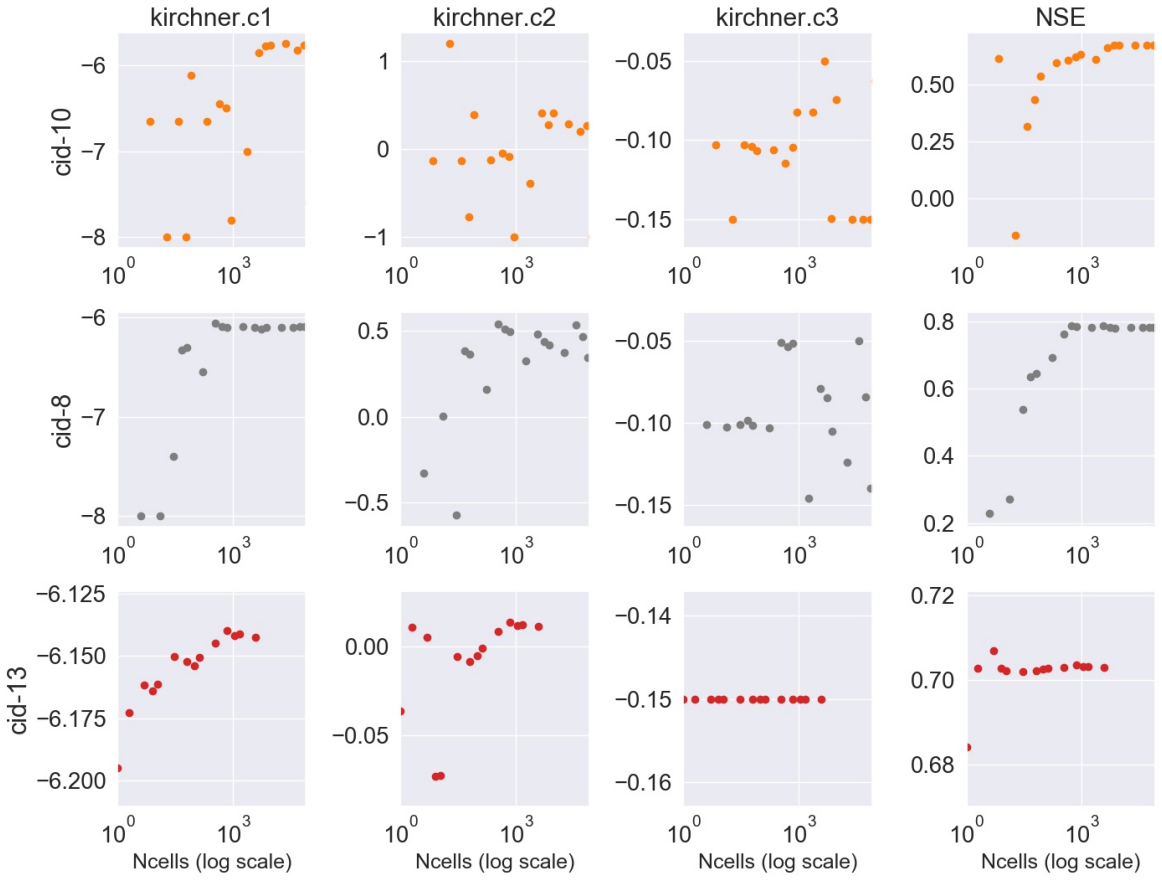

Figure 17. Kirchner parameters for subcatchments 10, 8 and 13

4.2 Radiation model

Correct simulation of snow melt and evapotranspiration requires knowledge of short-wave and long-wave radiation fluxes. However, radiation measurements are not always available. Furthermore, the instrumentation typically measure only fluxes on horizontal surface. For the low to middle resolution grids in order to overcome the limitations of on-ground data the general recommendation is to use satellite data with ordinary kriging for irradiance as the best option, followed by re-analysis products (Urraca et al., 2017, 2018). But when it comes to the grids and meshes with resolution less than 100 meters the satellite and reanalysis data has to be downscaled and further corrected for slope and aspect for mountainous regions.

The downscaling can be done, for example, following Fiddes and Gruber (2014), where the TopoScale model is clearly explained. Another way of downscaling shortwave radiation is described in Erlandsen et al. (2019), where authors perform

post-processing of ERA-Interim (Dee et al., 2011) for Norway using high-resolution, gridded 2 m temperature dataset (Lussana et al., 2018). One more option is to directly use (ESRI-ARCGIS, 2018) product. The general idea of it is to precalculate the viewshed, sunmap and sky map: the entire sky visible from the particular location is overlaid with the sun map (displays sun track variation during hours and days of year) and sky map (series of sky sectors defined by zenith and azimuth angles). This type of model was used in Nyman et al. (2014) with the satellite-based data downscaled to 20 m. The downscaling procedures are not covered in this study, as we consider the WFDEI reanalysis data with inverse distance weighting interpolation as being already satisfactory for our research (Bhattarai et al., 2020a)

As for translating onto inclined surfaces we have chosen the model by Allen et al. (2006) as the one being simple and robust. The original equations date back to Garnier and Ohmura (1970), Revfeim (1983) and Iqbal (1983). The simple idea is that one can scale direct normal irradiance with the cosine of solar zenith angle. This scaling factor is basically incorporated in many downscaling procedures and is studied a lot. For example, Tian et al. (2001) presented approach to estimate daily global radiation for any inclined surface with validation done in New Zealand. Ruiz-Arias et al. (2011) showed that downscaled and translated radiation improved simulations of WRF model up to 20% in southern Spain. Lopez-Moreno et al. (2013) considered Cold Region Hydrological Model (CRHM) which basically incorporates Garnier and Ohmura (1970) formulation to conduct a study in Pyrenees. The results showed that variability in snow accumulation and duration of snowpack is connected to slope and aspect distribution. Recent study by Aguilar et al. (2010) incorporates procedure by Allen et al. (2006) to study topographic effects on solar radiation and evapotranspiration in southern Spain with mesh resolution 30x30 m. Surface slope and aspect were calculated for each point in the DEM, using the regression plane through the 3x3 neighborhood of a given point after Dozier and Frew (1990). The comparison with experimental data showed practicality of the spatially distributed radiation in complex terrain. However, the need for the extra calculations caused by regular grid usage in order to obtain values for each cell is subject to computational costs, which are possible to avoid when using TIN meshes.

Furthermore, the model by Allen et al. (2006) satisfies Shyft requirement for arbitrary time step. Currently both instantaneous routine (numerically solving radiaiton at each time step) and the routine based on the integration during the period are implemented in Shyft. As Shyft is widely used in Northern latitudes, the situation with two periods of beam radiation during the day also considered in the implementation.

5 Conclusions

Final Remarks This study introduces a toolchain for hydrologic simulations on irregular triangular networks. Keeping in mind, that the whole purpose of Shyft is to be an efficient software for operational usage, we show the additional opportunities opened by discretization of the underlying region with triangular meshes. Rasputin software generates TIN-meshes with two options of land-cover. We demonstrate basic functionality of the software on the subcatchment Budhi-Gandaki of Narayani river in Nepal. The detailed description of mesh refinement, including analysis of geometry statistics and simple explanation of coarsening is presented. For the hydrologic simulations Rasputin meshes with various resolutions were generated for several subcatchments in the study area. The Shyft repository was updated with functions to parse Rasputin meshes and convert land

types to Shyft internal features. Experiments with various mesh resolutions demonstrate that even low-resolution TIN-mesh perform well. We also, clearly see that there is a limitation for Shyft to gain any improvement in terms of discharge simulation (NSE metric) with increased resolution of mesh. Experiments set B show a completely new routine of Shyft. Translation of radiation flux onto inclined surfaces unlocks a large set of possibilities within Shyft to study hillslopes hydrology. This routine is especially important when looking into snow simulation, as we now can clearly distinguish north and south facing slopes, revealing some well-known features of real world. The demonstrated results suggest that the detailed snow simulation will benefit from this improved radiation, though the discharge simulation efficiency would remain undisturbed. The presented experiments encourage the use of described toolchain as a computationally efficient way to study hydrology in mountainous regions.

The detailed analysis of performance of meshes of various resolutions leads to the recognition and understanding of hillslopes physical processes happening at the catchment scale. Understanding and controlling effects of topography are of considerable practical importance in operational cases, especially for snow dominated catchment. The flexibility of TIN-meshes allows capturing important features, while remaining computationally efficient. This study is our first step in assessing benefits for the practitioners in the power production industry, and the results are promising. Further study by Bhattarai et al. (2020b) gives more light on the usage of TIN-mesh for hydrological simulation.

6 Outlook

The current development of computational technologies allows hydrology practitioners to consider more physicalIy based distributed models as tools for day-to-day water related studies. However, there are many unresolved questions remain. The more complex models have more strict requirements to forcings and more practice in proper model configurations. Our results in the section 3.7 showed that we can't just propose tin-based configuration as a suitable (what are the metrics?) choice for practical problems, as we did in Bhattarai et al. (2020b), but need to force the users to analyse particular catchment in details, which is not always possible. Thus, as an outlook for this study we have a purpose to come with a recommendations for most efficient usage of Shyft in other regions with more variety of catchment types and climates.

Code and data availability. The current version of the Shyft model is available from the project website: https://gitlab.com/shyft-os/shyft under the GPLv.3 license. The documentation is available at https://gitlab.com/shyft-os/shyft-doc. The docker with exact version os Shyft and Rasputin valid for this publication is available at https://gitlab.com/shyft-os/dockers/-/tree/master/tin-pub. The exact version of the code of teh software used to produce the results in this paper is archived on Zenodo: Rasputin 0.3 alpha http://doi.org/10.5281/zenodo.3732351 and Shyft 4.9.1 http://doi.org/10.5281/zenodo.3732335. The scripts to run the model and produce the plots for all the simulations, including data collected during experiments presented in this paper are available at https://doi.org/10.5281/zenodo.3825570.

The hybrid dataset used for study in Narayani catchment is available at Bhattarai et al. (2019)

Appendix A: Resolution of land type datasets

The land types are assigned to each TIN based on the middle point position in the GlobCov 2009 (http://due.esrin.esa.int/page_globcover.php) or Corine (Europe) (https://land.copernicus.eu/global/products/) datasets with resolutions 300m and 80m respectively. In Figure A1 we show a TIN-mesh for the area around Finse, Norway with land types assigned from different sources. As can be seen for that particular area the Corine data is much more accurate. An equivalent high-resolution land type map is not available for our study site in Nepal to our knowledge. Also, as expected the water bodies have bigger cell areas and the hillslopes require more cells to get the representative terrain topography.

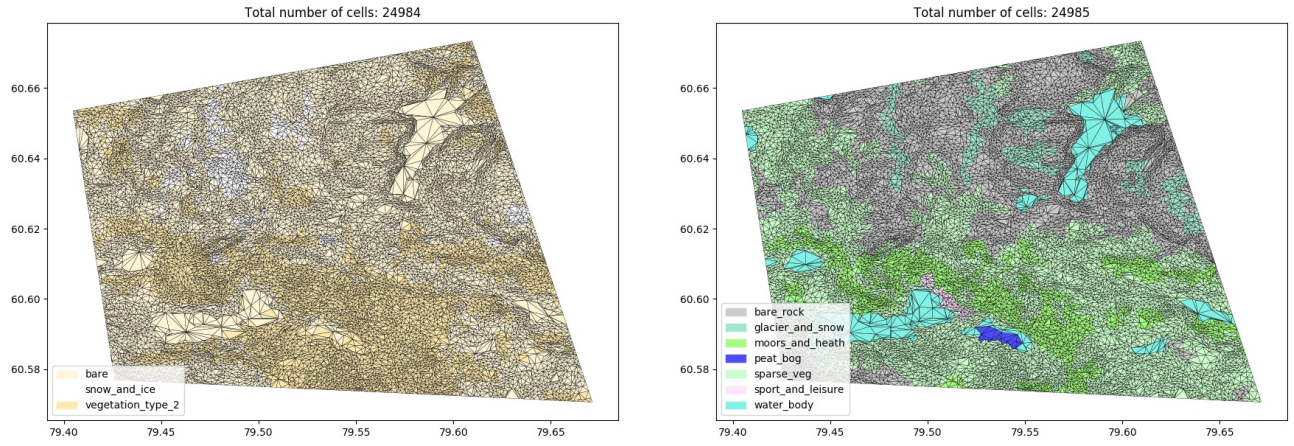

(a) (b)

Figure A1. Detail of TIN calculations using the a) GlovCov (300m) land type map, and b) Corine (80m) land type map for the region surrounding Finse, Norway.

Appendix B: PTGSK Model Stack

PT

The model calculates potential evapotranspiration with Priestley-Taylor method (Priestley and Taylor, 1972). The potential evapotranspiration PE can be estimated from the following equation:

$$PE_{PT} = \frac{\alpha_{PT}\Delta(S(1-pt.albedo)+L)}{\rho_w \lambda_\nu(\Delta+\gamma)}, \tag{B1}$$

where Δ is slope of saturation vapor pressure-temperature relation, S – incoming shortwave radiation and $pt.albedo$ is albedo, L – net long-wave radiation, ρ_w – water density, λ_ν – latent heat of vaporization, γ– psychrometric constant, $\alpha_{PT} = 1.26$ – a Priestley-Taylor coefficient, which is suitable for well-watered surfaces.

The actual evapotranspiration is calculated using scaling factor with a simple formulation:

$$AE = PE(1.0 - \exp(-Q \cdot 3.0/ae.scale\_factor)) \cdot (1.0 - SCF), \tag{B2}$$

where AE is actual evapotranspiration, $ae.scale\_factor$ is a scaling factor available for calibration, SCF – snow cover fraction.

GS

The gamma snow routine uses energy balance approach for snow ablation and snow depletion curve. The snow is distributed via three parameter gamma probability distribution. The net energy flux (ΔE) at the surface available for ablation can be written as:

$$\Delta E = S(1-\alpha) + L_{in} + L_{out} + H_{SE} + H_L + E_G, \tag{B3}$$

where S is net shortwave radiation flux, L is net longwave radiation flux, H_{SE}, H_L are sensible and latent heat fluxes, E_G is net ground heat flux calculated with a bulk-transfer approach, α is snow albedo. For a given timestep (t) α_t at each grid cell depends on minimum α_{min} and maximum α_{max} albedo values as well as the albedo decay rate, temperature and snowmelt (Hegdahl et al., 2016):

$$\alpha_t = \begin{cases} \alpha_{min} + (\alpha_{t-1} - \alpha_{min}) \cdot (\frac{1}{2^{\frac{1}{FADR}}}) & : T_\alpha \geq 0^o C \\ \alpha_{t-1} - (\alpha_{max} - \alpha_{min}) \cdot \frac{1}{2SADR} & : T_\alpha < 0^o C \end{cases}$$

where $FADR$ and $SADR$ denote fast and slow albedo decay rates in days, which are defined during calibration procedure. Other calibrating parameters for **GS** function are $tx, [^oC]$, which determines temperature threshold rain/snow for each grid cell, T_α – actual grid cell temperature, $wind\_scale, [-]$, which determines wind profile for the snow distribution. The snow is distributed using gamma probability,(Kolberg et al., 2006).

Snowmelt depth is calculated by multiplying available energy ΔE with the latent heat of fusion for water.

The glacier melt is happening with the simple temperature-index model (Hock, 2003). The snow in the grid cell melts first and only after that the glacier melt starts. The glacier reservoir is considered to be infinite and no change in glacier area is changing while simulations periods.

K

The catchment response function is a simple storage-discharge function, which determines the sensitivity of discharge to storage changes via fitting empirical function to the discharge timeseries. The nonlinearity and variability of the discharge led to the recommendation of using log transformed values in the numerical simulations. Thus, the relationship looks the following way:

$$\frac{d(\log Q)}{dt} = g(Q)\left(\frac{P-E}{Q} - 1\right), \tag{B4}$$

where P, Q, E are the rate of precipitation (either from snowmelt or rain), discharge and actual evapotranspiration from snow-free areas. The function $g(Q)$ can be estimated from the discharge timeserries and often take a form of quadratic equation:

$$g(Q) = \exp^{c1+c2(\log Q)+c3(\log Q)^2}, \tag{B5}$$

where $c1, c2, c3$ are the catchment specific parameters, which we call *kirchner* parameters. This parameters are obtained during calibration. Some considerations are presented in sec. 4.

Appendix C: Explanation of calibration parameters

Table C1. Calibration parameters for all experiments

Calibrated			
name	description	min	max
kirchner.c1	Outlet empirical coefficient 1, $[-]$	-8.0	0.0
kirchner.c2	Outlet empirical coefficient 2, $[-]$	-1.0	1.2
kirchner.c3	Outlet empirical coefficient 3, $[-]$	-0.15	-0.05
gs.tx	temperature rain/snow threshold, ^oC	-3.0	2.0
gs.wind_scale	slope in turbulent wind function, $[m/s]$	1.0	6.0
gs.FADR	fast albedo decay rate, $[days]$	5.0	15.0
gs.SADR	slow albedo decay rate, $[days]$	20.0	40.0
p_corr.scale_factor	precipitation scaling factor, $[-]$	0.2	2.0
rad.albedo[a]	surface albedo	0.1	1.0
rad.turbidity[a]	air turbidity, $[-]$	0.1	1.0
Constants			
name	description	value	
ae.ae_scale_factor	scale factor for actual evapotranspiration	1.0	
gs.max_water	fractional max water content of snow	0.1	
gs.wind_const	intercept in turbulent wind function	1.0	
gs.surface_magnitude	surface energy scaling factor	30	
gs.max_albedo	naximum snow albedo	0.9	
gs.min_albedo	minimum snow albedo	0.6	
gs.snowfall_reset_depth	depth of new snowfall at which snow albedo is reset, $[mm]$	5.0	
gs.snow_cv	spatial coefficient variation of new snow	0.4	
gs.snow_cv_forest_factor	modification factor snow_cv as function of forest fraction in cell	0	
gs.snow_cv_altitude_factor	modification factor for snow_cv as a function of altitude	0	
gs.glacier_albedo	albedo used for glacier areas	0.4	
gs.initial_bare_ground_fraction	initial bare ground fraction at melt onset	0.04	
gs.winter_end_day_of_year	last day of accumulation, $[day]$	70	
gs.n_winter_days	number of winter days, $[days]$	100	
pt.albedo	Priestley- Taylor albedo	0.2	
pt.alpha	Priestley-Taylor alpha	1.26	
gm.dtf	degree timstep factor for glacier melt, $[mm/day/^oC]$	6.0	
gm.direct_response	direct responce of glacier melt	0.475	
routing.velocity	routing speed, $[m/s]$	0.0	

[a] for RPTGSK stack only

Appendix D: Precipitation and Temperature Stations

For completeness we present here stations information from Bhattarai et al. (2020a).

Table D1. Temperature stations with names and locations

S.N	ID	Station name	Lat	Lon	Altitude, m.a.s.l
1	601	Jomsom	28.47	83.43	2744
2	607	Lete	28.38	83.36	2384
3	609	Benibajar	28.21	83.34	835
4	612	Mustang	29.13	83.58	3705
5	616	Gurja khani	28.36	83.13	2530
6	633	Chhoser	29.13	83.59	3870
7	706	Dumkauli	27.41	84.13	154
8	715	Khanchikot	27.56	83.09	1760
9	725	Tamghas	28.13	83.15	1530
10	802	Hudibajar	28.17	84.22	823
11	804	Pohara Airport	28.13	84.13	827
12	805	Syangja	28.13	83.53	868
13	809	Gorkha	28.32	84.37	1097
14	810	Chapkota	27.53	83.49	460
15	811	Malepatan(Phokhara)	28.14	84.07	856
16	814	Lumle	28.18	83.48	1740
17	817	Damauli	27.58	84.17	358
18	902	Rampur	27.37	84.25	256
19	905	Daman	27.36	85.05	2314
20	906	Hetauda	27.25	85.03	474
21	927	Bharatpur	27.13	84.26	205
22	1001	Timure	28.17	85.23	1900
23	1004	Nuwakot	27.55	85.1	1003
24	1005	Dhading	27.52	84.56	1420
25	1007	Kakani	27.48	85.15	2064
26	1022	Godavari	27.35	85.24	1400
27	1029	Khumaltar	27.13	85.2	1350
25	1038	Dhunibesi	27.43	85.11	1085
28	1039	Panipokhari	27.44	85.2	1335
29	1055	Dhunche	28.13	85.18	1982
30	1000	langtang	28.13	85.32	3670

Table D2. Precipitation stations with names and locations

S.N	ID	Station name	Lat	Lon	Altitude, m.a.s.l
1	601	Jomsom	28.78	83.71	2744
2	604	Thakmarpha	28.75	83.07	2566
3	605	Baglung	28.26	83.61	984
4	606	Tatopani	28.48	83.65	1243
5	609	Benibajar	28.35	83.56	835
6	610	Ghami	29.05	83.88	3465
7	612	Mustang	29.18	83.96	3705
8	613	karki neta	28.18	83.75	1720
9	614	Kusma	28.21	83.71	891
10	615	Bobang	28.04	83.15	2273
11	616	Gurja khani	28.06	83.21	2530
12	619	Ghorepani	28.04	83.73	2742
13	620	Tribeni	28.03	83.65	700
14	621	Darbang	28.38	83.41	1160
15	622	Rangkhani	28.15	83.56	1740
16	624	Samar Gaun	28.96	83.78	3570
17	625	Sanda	28.09	83.68	3570
18	626	Begha	28.46	83.61	1770
19	627	Kunun	28.38	83.48	1550
20	628	Muna	28.05	83.31	1970
21	629	Baghara	28.56	83.38	2330
22	630	Sirkon	28.13	83.61	790
23	701	Ridi Bajar	27.95	83.43	442
24	702	Palpa	27.86	83.53	1067
25	704	Beluwo	27.68	84.05	150
26	706	Dumkauli	27.68	84.22	154
27	715	Khanchikot	27.93	83.15	1760
28	716	kapilvastu	27.55	83.06	94
29	722	Musikot	28.01	83.26	1280
30	725	Tamghas	28.06	83.25	1530

Author contributions. Olga Silantyeva developed core radiation routine and new triangular cell representation, Rasputin repository in Shyft. Ola Skavhaug, Sigbjørn Helset and John F. Burkhart are core developers of Shyft. Ola Skavhaug and Magne Nordaas are main developers of Rasputin software. Bikas C. Bhattarai contributed to the discussions, data and experiments preparation. The original idea of the experiments

came from John F. Burkhart. All authors discussed the results. Olga took the lead in writing the paper with contributions from other authors. Lena M. Tallaksen participated in writing, review and editing.

Competing interests. The authors declare that they have no conflict of interest.

Acknowledgements. This work is a part of LATICE (Land Atmosphere Interaction in Cold Environments) project at the University of Oslo.

References

Addor, N., Newman, A. J., Mizukami, N., and Clark, M. P.: The CAMELS data set: catchment attributes and meteorology for large-sample studies, Hydrology and Earth System Sciences, 21, 5293–5313, https://doi.org/10.5194/hess-21-5293-2017, https://www.hydrol-earth-syst-sci.net/21/5293/2017/, 2017.

Aguilar, C., Herrero, J., and Polo, M. J.: Topographic effects on solar radiation distribution in mountainous watersheds and their influence on reference evapotranspiration estimates at watershed scale, Hydrology and Earth System Sciences, 14, 2479–2494, 2010.

Allen, R. G., Trezza, R., and Tasumi, M.: Analytical integrated functions for daily solar radiation on slopes, Agricultural and Forest Meteorology, 139, 55–73, 2006.

Bajracharya, S. R., Maharjan, S. B., Shrestha, F., Bajracharya, O., and Baidya, S.: Glacier Status in Nepal and Decadal Change from 1980 to 2010 Based on Landsat Data, Tech. rep., International Centre for Integrated Mountain Development, GPO Box 3226, Kathmandu, Nepal, 2014.

Bhattarai, B. C., Burkhart, J. F., Tallaksen, L. M., Xu, C.-Y., and Matt, F. N.: Evaluation of global forcing data sets for hydropower inflow simulation in Nepal, Hydrology Research, https://doi.org/10.5281/zenodo.3567830, https://doi.org/10.5281/zenodo.3567830, 2019.

Bhattarai, B. C., Burkhart, J. F., Tallaksen, L. M., Xu, C.-Y., and Matt, F. N.: Evaluation of global forcing datasets for hydropower inflow simulation in Nepal, Hydrology Research, 51, 202–225, https://doi.org/10.2166/nh.2020.079, https://doi.org/10.2166/nh.2020.079, 2020a.

Bhattarai, B. C., Silantyeva, O., Teweldebrhan, A. T., Helset, S., Skavhaug, O., and Burkhart, J. F.: Impact of Catchment Discretization and Imputed Radiation on Model Response: A Case Study from Central Himalayan Catchment, Water, 12, 2020b.

Bhuju, D. R., McLaughlin, K., Sijapati, J., Devkota, B. D., Shrestha, N., Ghimire, G. P., and Neupane, P. K.: Building Knowledge for Climate Resilience in Nepal Research Briefs, Tech. rep., Nepal Academy of Science and Technology, 2016.

Boissonnat, J.-D., Devillers, O., Pion, S., Teillaud, M., and Yvinec, M.: Triangulations in CGAL, Computational Geometry: Theory and Applications, 22, 5–19, 2002.

Boissonnat, J.-D., Devillers, O., and Hornus, S.: Incremental construction of the Delaunay graph in medium dimension., in: Proceedings of the 25th Annual Symposium on Computational Geometry, edited by Aarhus, D., pp. 208–216, 2009.

Boissonnat, J.-D., Devillers, O., Dutta, K., and Glisse, M.: Randomized incremental construction of Delaunay triangulations of nice point sets, hal, 2019.

Bookhagen, B. and Burbank, D. W.: Toward a complete Himalayan hydrological budget: Spatiotemporal distribution of snowmelt and rainfall and their impact on river discharge, Journal of Geophysical Research, 115, 2010.

Bowyer, A.: Computing Dirichlet tessellations, The Computer Journal, 24, 162–166, 1981.

Budhigandaki Hydroelectric Project Development Commitee (BHPDC): Feasibility Study and detailed design of Budhi Gandaki HPP. Phase 3. Final Detailed Design Report, Tech. rep., Tractebel Engineering and Coyne et Bellier and Jade Consult, 2015.

Burkhart, J. F., Helset, S., Abdella, Y. S., and Lappegard, G.: Operational Research:Evaluating Multimodel Implementations for 24/7 Runtime Environment, American Geophysical Union, Fall General Assembly 2016, Abstract Id. H51F-1541, 2016.

Burkhart, J. F., Matt, F. N., Helset, S., Sultan Abdella, Y., Skavhaug, O., and Silantyeva, O.: Shyft v4.8: a framework for uncertainty assessment and distributed hydrologic modeling for operational hydrology, Geoscientific Model Development, 14, 821–842, https://doi.org/10.5194/gmd-14-821-2021, https://gmd.copernicus.org/articles/14/821/2021/, 2021.

Carey, S. K. and Woo, M.-k.: Spatial variability of hillslope water balance, wolf creek basin, subarctic yukon, Hydrological Processes, 15, 3113–3132, 2001.

Clark, M. P., Hendrikx, J., Slater, A. G., Kavetski, D., Anderson, B., Cullen, N. J., Kerr, T., Hreinsson, E. Ö., and Woods, R. A.: Representing spatial variability of snow water equivalent in hydrologic and land-surface models : A review, Water Resources Research, 47, https://doi.org/10.1029/2011WR010745, 2011.

Comola, F., Schaefli, B., Ronco, P., Botter, G., Bavay, M., Rinaldo, A., and Lehning, M.: Scale-dependent effects of solar radiation patterns on the snow-dominated hydrologic response, Geophysical Research Letters, 42, 3895–3902, 2015.

Dee, D. P., Uppala, S. M., Simmons, A. J., Berrisford, P., Poli, P., Kobayashi, S., Andrae, U., Balmaseda, M. A., Balsamo, G., Bauer, P., Bechtold, P., Beljaars, A. C. M., van de Berg, L., Bidlot, J., Bormann, N., Delsol, C., Dragani, R., Fuentes, M., Geer, A. J., Haimberger, L., Healy, S. B., Hersbach, H., Hólm, E. V., Isaksen, L., Kållberg, P., Köhler, M., Matricardi, M., McNally, A. P., Monge-Sanz, B. M., Morcrette, J.-J., Park, B.-K., Peubey, C., de Rosnay, P., Tavolato, C., Thépaut, J.-N., and Vitart, F.: The ERA-Interim reanalysis: configuration and performance of the data assimilation system, Quarterly Journal of the Royal Meteorological Society, 137, 553–597, https://doi.org/10.1002/qj.828, https://rmets.onlinelibrary.wiley.com/doi/abs/10.1002/qj.828, 2011.

Devillers, O.: Improved Incremental Randomized Delaunay Triangulations, arXiv, 1999.

Devillers, O. and Teillaud, M.: Perturbations for Delaunay and weighted Delaunay 3D Triangulations, Computational Geometry, 44, 160–168, 2011.

Dozier, J. and Frew, J.: Rapid calculation of terrain parameters for radiation modeling from digital elevation data, IEEE Transactions on Geoscience and Remote Sensing, 1990.

Erlandsen, H. B., Tallaksen, L. M., and Kristiansen, J.: Merits of novel high-resolution estimates and existing long-term estimates of humidity and incident radiation in a complex domain, Earth System Science Data, 11, 797–821, https://doi.org/10.5194/essd-11-797-2019, https://www.earth-syst-sci-data.net/11/797/2019/, 2019.

ESRI-ARCGIS: http://desktop.arcgis.com/en/arcmap/10.3/tools/spatial-analyst-toolbox/an-overview-of-the-solar-radiation-tools.htm, Tech. rep., 2018.

Fan, Y., Clark, M., Lawrence, D. M., Swenson, S., Band, L. E., Brantley, S. L., Brooks, P. D., Dietrich, W. E., Flores, A., Grant, G., Kirchner, J. W., Mackay, D. S., McDonnell, J. J., Milly, P. C. D., Sullivan, P. L., Tague, C., Ajami, H., Chaney, N., Hartmann, A., Hazenberg, P., McNamara, J., Pelletier, J., Perket, J., Rouholahnejad-Freund, E., Wagener, T., Zeng, X., Beighley, E., Buzan, J., Huang, M., Livneh, B., Mohanty, B. P., Nijssen, B., Safeeq, M., Shen, C., van Verseveld, W., Volk, J., , and Yamazaki, D.: Hillslope Hydrology in Global Change Research and Earth System Modeling, Water Resources Research, 55, 2019.

Fiddes, J. and Gruber, S.: TopoSCALE v.1.0: downscaling gridded climate data in complex terrain, Geoscientific Model Development, 2014.

Fogel, E. and Teillaud, M.: The Computational Geometry Algorithms Library CGAL, ACM Communications in Computer Algebra, 47, 85–87, 2013.

Garnier, B. and Ohmura, A.: The evaluation of surface variations in solar radiation income, Solar energy, 13, 21–34, 1970.

Gupta, H. V., Kling, H., Yilmaz, K. K., and Martinez, G. F.: Decomposition of the mean squared error and NSE performance criteria: Implications for improving hydrological modelling, Journal of Hydrology, 377, 80–91, 2009.

Hegdahl, T. J., Tallaksen, L. M., Engeland, K., Burkhart, J. F., and Xu, C.-Y.: Discharge sensitivity to snowmelt parameterization: a case study for Upper Beas basin in Himachal Pradesh, India, Hydrology Research, 47, https://doi.org/10.2166/nh.2016.047, 2016.

Hock, R.: Temperature index melt modeling in mountain areas, Journal of Hydrology, 282, https://doi.org/10.1016/S0022-1694(03)00257-9, 2003.

Iqbal, M.: An introduction to Solar Radiation, Academic Press, New-York, 1983.

Ivanov, V. Y., Vivoni, E. R., Bras, R. L., and Entekhabi, D.: Preserving high-resolution surface and rainfall data in operational-scale basin hydrology: a fully-distributed physically-based approach, Journal of Hydrology, 298, 80–111, 2004.

Jakob, W., Rhinelander, J., and Moldovan, D.: pybind11 – Seamless operability between C++11 and Python, https://github.com/pybind/pybind11, 2017.

Kettner, L., Mehlhorn, K., Pion, S., Schirra, S., and Yap, C.: Classroom examples of robustness problems in geometric computations, Computational Geometry: Theory and Applications, 40, 61–78, 2008.

Kirchner, J. W.: Catchments as simple dynamical systems: Catchmentcharacterization, rainfall-runoff modeling, and doing hydrologybackward, Water Resources Research, 45, https://doi.org/10.1029/2008WR006912, 2009.

Kolberg, S., Rue, H., and Gottschalk, L.: A Bayesian spatial assimilation scheme for snow coverage observations in a gridded snow model, Hydrology and Earth System Science, 10, 369–381, https://doi.org/10.5194/hess-10-369-2006, 2006.

Kripalani, R. H., Inamdar, S., and Sontakke, N. A.: Rainfall variability over Bangladesh and Nepal: Comparison and connections with features over India, Int. J. Climatol., 16, 689–703, https://doi.org/10.1002/(SICI)1097-0088(199606)16:6<689::AID-JOC36>3.0.CO;2-K, 1996.

Kumar, M., Bhatt, G., and Duffy, C. J.: An efficient domain decomposition framework for accurate representation of geodata in distributed hydrologic models, International Journal of Geographical Information Science, 23, 1569–1596, 2009.

Liang, X., Lettenmaier, D. P., Wood, E. F., and Burges, S. J.: A simple hydrologically based model of land surface water and energy fluxes for general circulation models, Journal of Geophysical Research: Atmospheres, 99, 14 415–14 428, https://doi.org/10.1029/94JD00483, https://agupubs.onlinelibrary.wiley.com/doi/abs/10.1029/94JD00483, 1994.

Lindstrom, P. and Turk, G.: Fast and memory efficient polygonal simplification, IEEE Visualization, pp. 279–286, 1998.

Lindstrom, P. and Turk, G.: Evaluation of memoryless simplification, IEEE Transactions on Visualization and Computer Graphics, 5, 98–115, 1999.

Liu, Y. and Snoeyik, J.: A Comparison of Five Implementations of 3D Delaunay Tessellation, Combinatorial and Computational Geometry, 52, 439–458, 2005.

Lopez-Moreno, J. I., Revuelto, J., Gilaberte, M., Moran-Tejeda, E., Pons, M., Jover, E., Esteban, P., García, C., and Pomeroy, J. W.: The effect of slope aspect on the response of snowpack to climate warming in the Pyrenees, Theoretical and Applied Climatology, 117, 207–219, 2013.

Lussana, C., Tveito, O. E., and Uboldi, F.: Three-dimensional spatial interpolation of 2 m temperature over Norway, Quarterly Journal of the Royal Meteorological Society, 144, 344–364, https://doi.org/10.1002/qj.3208, https://rmets.onlinelibrary.wiley.com/doi/abs/10.1002/qj.3208, 2018.

Marsh, C. B., Spiteri, R. J., Pomeroy, J. W., and Wheater, H. S.: Multi-objective unstructured triangular mesh generation for use in hydrological and land surface models, Computers and Geosciences, 119, 49–67, 2018.

Marsh, C. B., Pomeroy, J. W., and Wheater, H. S.: The Canadian Hydrological Model (CHM) v1.0: a multi-scale, multi-extent, variable-complexity hydrological model – design and overview, Geoscientific Model Development, 13, 225–247, https://doi.org/10.5194/gmd-13-225-2020, https://www.geosci-model-dev.net/13/225/2020/, 2020.

Nash, J. and Sutcliffe, J.: River flow forecasting through conceptual models part I — A discussion of principles, Journal of Hydrology, 10, 282–290, 1970.

Newman, A., Sampson, K., Clark, M. P., Bock, A., Viger, R. J., and Blodgett, D.: A large-sample watershed-scale hydrometeorological dataset for the contiguous USA, https://doi.org/https://dx.doi.org/10.5065/D6MW2F4D, 2014.

Nyman, P., B.Sherwin, C., Langhans, C., Lane, P. N., and Sheridan, G. J.: Downscaling regional climate data to calculate the radiative index of dryness in complex terrain, Australian Meteorolical and Oceanographic Journal, 64, 109–122, 2014.

Omani, N., Srinivasan, R., Karthikeyan, R., and Smith, P.: Hydrological modeling of highly glacierized basins (Andes, Alps, and Central Asia)., Water, 9, 111, https://doi.org/10.3390/w9020111, 2017.

Peuckert, K., Flowerrr, L., Little, J., and Markd, M.: Digital Representation of Three-dimensional Surfaces by Triangulated Irregular Networks (TIN), Technical Report Number 10, United State Offiec of Naval Research, Geography Programms, 1976.

Picard, G., Dumont, M., Lamare, M., Tuzet, F., Larue, F., Pirazzini, R., and Arnaud, L.: Spectral albedo measurements over snow-covered slopes: theory and slope effect corrections, Cryosphere, Discussion, 2020.

Priestley, C. and Taylor, R.: On the Assessment of Surface Heat Flux and Evaporation Using Large-Scale Parameters, Monthly Weather Reiew, 100, 81–92, https://doi.org/10.1175/1520-0493(1972)100<0081:OTAOSH>2.3.CO;2, 1972.

Revfeim, K.: A simple procedure for estimating global daily radiation on any surface, Journal of Applied Meteorology, 17, 1126–1131, 1983.

Ruiz-Arias, J. A., Pozo-Vazques, D., Lara-Fanego, V., Santos-Alamillos, F. J., and Tovar-Pescador, J.: A High-Resolution Topographic Correction Method for Clear-Sky Solar Irradiance Derived with a Numerical Weather Prediction Model, Journal of Applied Meteorology and Climatology, 50, 2460–2472, 2011.

Sanderson, C. and Curtin, R.: Armadillo: a template-based C++ library for linear algebra, Journal of Open Source Software, 1, 26, https://doi.org/10.21105/joss.00026, https://doi.org/10.21105/joss.00026, 2016.

Sanderson, C. and Curtin, R.: A User-Friendly Hybrid Sparse Matrix Class in C++, in: Mathematical Software – ICMS 2018, edited by Davenport, James H.and Kauers, M., Labahn, G., and Urban, J., pp. 422–430, Springer International Publishing, Cham, https://doi.org/10.1007/978-3-319-96418-8_50, 2018.

Schlömer, N., McBain, G., Luu, K., christos, Li, T., Ferrándiz, V. M., Barnes, C., Dalcin, L., eolianoe, nilswagner, Lukeš, V., Gupta, A., Müller, S., Schwarz, L., Blechta, J., Coutinho, C., Beurle, D., Dokken, J. S., s1291, Villa, U., mrambausek, Cereijo, I., Shrimali, B., Cervone, A., lgiraldi, Jacquenot, G., Vaillant, G. A., Wilson, C., Gudchenko, A. U., and Croucher, A.: nschloe/meshio v4.0.12, https://doi.org/10.5281/zenodo.3773318, https://doi.org/10.5281/zenodo.3773318, 2020.

Seiller, G., Anctil, F., and Perrin, C.: Multimodel evaluation of twenty lumped hydrological models under contrasted climate conditions, Hydrology and Earth Science, 16, 1171–1189, 2012.

Shepard, D.: A two-dimensional interpolation function for irregularly spaced data, in: Proceedings of the 1968 23rd ACM national conference, 1968.

Teweldebrhan, A. T., Burkhart, J. F., and Schuler, T. V.: Parameter uncertainty analysis for an operational hydrological model using residual-based and limits of acceptability approaches, Hydrology and Earth System Science, 22, 5021–5039, 2018.

Tian, Y., Davies-Colley, R., Gong, P., and Thorrold, B.: Estimating Solar Radiation on Slopes of Arbitrary Aspect, Agricultural and Forest Meteorology, 109, 67–74, 2001.

Tsai, V. J. D.: Delaunay triangulations in TIN creation: an overview and a linear-time algorithm, International Journal of Geographical Information Science, 7, 501–524, 1993.

Urraca, R., de Pison, E. M., Sanz-Garcia, A., Antonanzas, J., and Antonanzas-Torres, F.: Estimation methods for global solar radiation: Case study evaluation of five different approaches in central Spain, Renewable and Sustainable Energy Reviews, 77, 1098–1113, https://doi.org/10.1016/j.rser.2016.11.222, 2017.

Urraca, R., Thomas, H., Gracia-Amillo, A., Martinez-de Pisona, F. J., Kaspar, F., and Sanz-Garcia, A.: Evaluation of global horizontal irradiance estimates from ERA5 and COSMO-REA6 reanalyses using ground and satellite-based data, Solar Energy, 164, 339–354, 2018.

Weedon, G. P., Balsamo, G., Bellouin, N., Gomes, S., Best, M. J., and Viterbo, P.: The WFDEI meteorological forcing data set: WATCH Forcing Data methodology applied to ERA-Interim reanalysis data, Water Resources Research, 50, https://doi.org/10.1002/2014WR015638, 2014.